A mechanism-based multi-trap phase field model for hydrogen assisted fracture

Mehrdad Isfandbod[a], Emilio Martínez-Pañeda[a,*]

[a]*Department of Civil and Environmental Engineering, Imperial College London, London SW7 2AZ, UK*

Abstract

We present a new mechanistic, phase field-based formulation for predicting hydrogen embrittlement. The multi-physics model developed incorporates, for the first time, a Taylor-based dislocation model to resolve the mechanics of crack tip deformation. This enables capturing the role of dislocation hardening mechanisms in elevating the tensile stress, hydrogen concentration and dislocation trap density within tens of microns ahead of the crack tip. The constitutive strain gradient plasticity model employed is coupled to a phase field formulation, to simulate the fracture process, and to a multi-trap hydrogen transport model. The analysis of stationary and propagating cracks reveals that the modelling framework presented is capable of adequately capturing the sensitivity to the hydrogen concentration, the loading rate, the material strength and the plastic length scale. In addition, model predictions are compared to experimental data of notch tensile strength versus hydrogen content on a high-strength steel; a very good agreement is attained. We define and implement both atomistic-based and phenomenological hydrogen

---

*Corresponding author.
Email address: e.martinez-paneda@imperial.ac.uk (Emilio Martínez-Pañeda)

degradation laws and discuss similarities, differences and implications for the development of parameter-free hydrogen embrittlement models.

1. Introduction

The ingress of hydrogen into a metal is known to cause a dramatic reduction in material strength, ductility, toughness and fatigue resistance (Gangloff, 2003). This phenomenon, referred to as hydrogen embrittlement, has attracted the attention of the material science and solid mechanics communities for decades due to its important technological implications and the scientific challenges inherent to its complex chemo-micromechanical nature (Djukic et al., 2019). Moreover, the problem has come very much to the fore in recent years as a consequence of the higher susceptibility of new, high-strength alloys, and because of the promise that hydrogen holds as a future energy carrier, requiring the development of suitable structures for hydrogen storage and transport (Gangloff and Somerday, 2012; Paxton et al., 2017).

A notable effort has been devoted to the development of multi-physics models for predicting hydrogen assisted failures; despite the complexity of understanding and reproducing the underlying mechanisms, which span multiple scales and can vary significantly from one material to another (Dadfarnia et al., 2010; Harris et al., 2018; Lynch, 2019; Shishvan et al., 2020; Kristensen et al., 2020a). A wide variety of continuum-like models have been presented

2

to predict and couple the multiple elements of this phenomenon: the deformation of the solid, the uptake and diffusion of hydrogen through the crystal lattice, and the resulting hydrogen assisted damage. The constitutive behaviour of the solid is typically characterised by using conventional von Mises plasticity theory, occasionally incorporating the effects of hydrogen-induced dilatation (Lufrano et al., 1998) and hydrogen-induced softening (Díaz et al., 2016). Recently, there has been a growing interest in enriching the constitutive behaviour using strain gradient plasticity, so as to provide a more accurate description of crack tip fields by incorporating the influence of Geometrically Necessary Dislocations (GNDs) and plastic strain gradients (Martínez-Pañeda et al., 2016; Kumar and Mahajan, 2020). In regard to hydrogen transport, models based on Fickian diffusion have been developed to capture bulk transport (Van Leeuwen, 1974), and subsequently extended to capture stress-assisted diffusion and the role of microstructural traps in retaining hydrogen. These models take as primal kinematic variable either the lattice hydrogen concentration (Sofronis and McMeeking, 1989; Barrera et al., 2016; Fernández-Sousa et al., 2020) or the chemical potential (Di Leo and Anand, 2013; Elmukashfi et al., 2020). In addition, generalised boundary conditions have been proposed to resolve the electrochemical-diffusion interface (Martínez-Pañeda et al., 2020a), in a first step to quantifying not only hydrogen diffusion but also ingress (Kehler and Scully, 2008). Finally, coupled deformation-diffusion models have been extended to explicitly predict hydrogen-assisted crack initiation and growth. The vast majority of these models are based on the concept of a fracture process zone, with hydrogen degrading the fracture energy of the solid. The most popular methodology

3

has arguably been the use of cohesive zone models; see, e.g., (Serebrinsky et al., 2004; Yu et al., 2016; del Busto et al., 2017) and Refs. therein. However, phase field fracture models have recently been proposed to overcome the limitations intrinsic to cohesive zone formulations and other discrete methods. The phase field has emerged as a promising variational tool for fracture; enabling capturing - on the original finite element mesh and in arbitrary geometries and dimensions - complex cracking phenomena such as crack nucleation, branching, kinking or merging (Bourdin et al., 2000; Duda et al., 2015; Miehe et al., 2016; Kristensen and Martínez-Pañeda, 2020; Simoes and Martínez-Pañeda, 2021). This success has recently been extended to hydrogen embrittlement, with multi-physics phase field fracture formulations quickly gaining traction, and demonstrating their ability to reproduce experimental results and predict failures in service conditions (Martínez-Pañeda et al., 2018; Duda et al., 2018; Martínez-Pañeda et al., 2020b; Wu et al., 2020a; Kristensen et al., 2020b).

In this work, we present a new phase field-based formulation for hydrogen assisted cracking. The model incorporates, for the first time, the influence of hydrogen traps in a phase field framework. Multiple trap types are considered, capturing their influence on diffusion and fracture. Moreover, phase field fracture is coupled with a mechanism-based strain gradient plasticity model, also for the first time. This is of notable importance as it provides an enriched description of crack tip fields over the critical length scale for hydrogen damage. Consider for example the fracture experiments on Monel K500 reported in (Martínez-Pañeda et al., 2016); the crack growth rate in stage

4

II ($\mathrm{d}a/\mathrm{d}t_{II}$), where cracking is intermittent and $\mathrm{d}a/\mathrm{d}t$ is constant (diffusion-controlled), is on the order of 0.04 µm/s for three replicate experiments under an applied potential of $E_A = -1000$ mV_{SCE}. Given that the diffusion distance can be approximated as $d = 2\sqrt{Dt}$, with Monel K500 having a diffusion coefficient $D = 0.01$ µm^2/s, this results in a critical distance of $x_{crit} \sim 1$ µm. It is well known that conventional continuum models fail to capture the dislocation hardening mechanisms governing material deformation at the micro-scale. Of particular relevance to cracks in engineering components is the flow stress elevation associated with plastic strain gradients and large dislocation densities, as measured under similar conditions using indentation or a plethora of micro-scale experiments; from micro-torsion to constrained shear of thin films (Fleck et al., 1994; Tvergaard and Niordson, 2004; Gurtin and Anand, 2005; Mu et al., 2014; Voyiadjis and Song, 2019). The plastic zone adjacent to the crack tip is physically small and contains large gradients of plastic strain, leading to local strengthening and a stress elevation that can have important implications for hydrogen embrittlement, given the exponential dependence of the hydrogen concentration on hydrostatic stresses and the central role that crack tip stresses play in triggering interface decohesion (Wei and Hutchinson, 1997; Wei and Xu, 2005; Komaragiri et al., 2008; Martínez-Pañeda and Betegón, 2015; Martínez-Pañeda and Niordson, 2016). In addition, the dislocation trap density near the crack tip could be larger than that predicted by conventional continuum theories, due to the GNDs contribution. These features are captured here by means of a formulation based on Taylor (1938) dislocation density model.

The remainder of this paper is organised as follows. In Section 2 we present our theoretical framework. Then, the finite element implementation is described in Section 3. Representative numerical results are shown in Section 4. First, a boundary layer model is used to gain insight into crack initiation and growth under small scale yielding conditions. Secondly, we compare the predictions of our model with experiments conducted on high-strength alloys exposed to hydrogenous environments. Concluding remarks end the paper in Section 5.

Notation. We use lightface italic letters for scalars, e.g. ϕ, upright bold letters for vectors, e.g. $\mathbf{u}$, and bold italic letters, such as $\boldsymbol{\sigma}$, for second and higher order tensors. Inner products are denoted by a number of vertically stacked dots, corresponding to the number of indices over which summation takes place, such that $\boldsymbol{\sigma} : \boldsymbol{\varepsilon} = \sigma_{ij}\varepsilon_{ij}$, with indices referring to a Cartesian coordinate system. The gradient and the Laplacian are respectively denoted by $\nabla \mathbf{u} = u_{i,j}$ and $\Delta\phi = \phi_{,ii}$. Finally, divergence is denoted by $\nabla \cdot \boldsymbol{\sigma} = \sigma_{ij,j}$, the trace of a second order tensor is written as $\operatorname{tr}\boldsymbol{\varepsilon} = \varepsilon_{ii}$, and the deviatoric part of a tensor is written as $\boldsymbol{\sigma}' = \sigma_{ij} - \delta_{ij}\sigma_{kk}/3$, with δ_{ij} denoting the Kronecker delta.

2. Theory

In this section, we formulate our theory, which couples deformation, fracture and hydrogen transport in strain gradient plasticity solids. The theory refers to the response of a body occupying an arbitrary domain $\Omega \subset \mathbb{R}^n$ ($n \in [1, 2, 3]$), with external boundary $\partial\Omega \subset \mathbb{R}^{n-1}$, on which the outwards

6

unit normal is denoted as $\mathbf{n}$. In the following, we restrict our attention to isothermal conditions and isotropic solids.

2.1. Kinematics

We shall now discuss the independent fields that will be used to describe the kinematical structure of Ω. In regard to the deformation of the solid, the motion of a material point $\mathbf{x}$ at a time t is characterised by a displacement vector field $\mathbf{u}(\mathbf{x}, t)$. Such that, assuming a small strain formulation, the local deformation is determined by the infinitesimal strain tensor field $\boldsymbol{\varepsilon}$; given by

$$\boldsymbol{\varepsilon} = \frac{1}{2} \left(\nabla \mathbf{u}^T + \nabla \mathbf{u} \right).$$ (1)

Our constitutive theory considers both elastic and plastic strains, adopting the standard partition:

$$\boldsymbol{\varepsilon} = \boldsymbol{\varepsilon}^e + \boldsymbol{\varepsilon}^p.$$ (2)

The nucleation and growth of cracks are described by means of a phase field variable, or order parameter, $\phi(\mathbf{x}, t) \in [0, 1]$. Following standard damage mechanics arguments, the phase field equals $\phi = 0$ for intact material and $\phi = 1$ for fractured material points. Using a phase field auxiliary variable to *implicitly* track interfaces has opened new horizons in the modelling of fracture (Wu et al., 2020b), microstructural evolution (Provatas and Elder, 2011), and metal corrosion (Cui et al., 2021). Here, in the context of fracture, the phase field variable must grow monotonically,

$$\dot{\phi}(\mathbf{x}, t) \geq 0,$$ (3)

so as to ensure that the microstructural changes associated with damage are irreversible.

7

In addition, we consider the changes in composition of material points in Ω. The presence of guest hydrogen atoms in a host metallic lattice is characterised by the hydrogen concentration $C(\mathbf{x}, t)$. Here, $C(\mathbf{x}, t)$ denotes the total number of moles of hydrogen atoms per unit reference volume. Even though mass concentration is the sought variable, the thermodynamic driving force for diffusion is the chemical potential gradient $\nabla \mu$. As in Duda et al. (2018), we define a scalar field $\eta(\mathbf{x}, t)$ to determine the kinematics of composition changes, such that

$$\dot{\eta} = \mu \quad \text{and} \quad \eta(\mathbf{x}, t) = \int_0^t \mu(\mathbf{x}, t) \, \mathrm{d}t \,. \tag{4}$$

2.2. Principle of virtual work. Balance of forces

We shall now derive the balance equations for the coupled system using the principle of virtual work. Consider the three-field boundary value problem resulting from the primal kinematic variables described before: $\mathbf{u}$, ϕ, and η. The Cauchy stress $\boldsymbol{\sigma}$ is introduced, which is work conjugate to the strain tensor $\boldsymbol{\varepsilon}$. Correspondingly, for an outwards unit normal $\mathbf{n}$ on the boundary $\partial \Omega$ of the solid, a vector traction $\mathbf{T}$ is defined, which is work conjugate to the displacement field $\mathbf{u}$. The damage response involves a scalar stress-like quantity ω, which is work conjugate to the phase field ϕ, and a phase field micro-stress vector $\boldsymbol{\xi}$ that is work conjugate to the gradient of the phase field $\nabla \phi$. The phase field is assumed to be driven by the displacement problem alone; i.e., no external traction is associated with ϕ. In regard to the mass transport, the surface flux is denoted by $\mathbf{J}$, and accordingly, a concentration flux entering the body across $\partial \Omega$ can be defined as $q = \mathbf{J} \cdot \mathbf{n}$. Then, making use of three virtual fields ($\delta \mathbf{u}$, $\delta \phi$, $\delta \eta$), the principle of virtual work for the

8

coupled system reads,

$$\int_{\Omega} \left(\boldsymbol{\sigma} : \delta\boldsymbol{\varepsilon} + \omega\,\delta\phi + \boldsymbol{\xi} \cdot \nabla\delta\phi - \dot{C}\,\delta\eta + \mathbf{J} \cdot \nabla\delta\eta \right)\,\mathrm{d}V = \int_{\partial\Omega} (q\,\delta\eta + \mathbf{T} \cdot \delta\mathbf{u})\,\mathrm{d}S$$

(5)

The principle of virtual work must hold for an arbitrary domain Ω and for any kinematically admissible variations of the virtual quantities. Thus, by making use of Gauss's divergence theorem, the local force balances are obtained as:

$$\nabla \cdot \boldsymbol{\sigma} = 0$$
$$\nabla \cdot \boldsymbol{\xi} - \omega = 0 \qquad \text{in } \Omega,$$
$$\dot{C} + \nabla \cdot \mathbf{J} = 0$$

(6)

with natural boundary conditions:

$$\boldsymbol{\sigma} \cdot \mathbf{n} = \mathbf{T}$$
$$\boldsymbol{\xi} \cdot \mathbf{n} = 0 \qquad \text{on } \partial\Omega.$$
$$q = \mathbf{J} \cdot \mathbf{n}$$

(7)

2.3. Energy imbalance

We shall now impose the first and second laws of thermodynamics through an energy imbalance. The first two laws of thermodynamics for a continuum body within a dynamical process of specific internal energy $\mathscr{E}$ and specific entropy Λ read (Gurtin et al., 2010),

$$\frac{\mathrm{d}}{\mathrm{d}t}\int_{\Omega} \mathscr{E}\,\mathrm{d}V = \dot{W}_e\,(\Omega) - \int_{\partial\Omega} \mathbf{Q} \cdot \mathbf{n}\,\mathrm{d}S + \int_{\Omega} Q\,\mathrm{d}V$$
$$\frac{\mathrm{d}}{\mathrm{d}t}\int_{\Omega} \Lambda\,\mathrm{d}V \geqslant -\int_{\partial\Omega} \frac{\mathbf{Q}}{T} \cdot \mathbf{n}\,\mathrm{d}S + \int_{\Omega} \frac{Q}{T}\,\mathrm{d}V\,.$$

(8)

Here, $\dot{W}_e$ is the power of external work, $\mathbf{Q}$ is the heat flux, and Q is the heat absorption. The thermodynamic laws in the presence of species transport

9

require that the temporal increase in free energy of any part Ω is less than or equal to the power expended on Ω plus the flux of energy carried into Ω through its boundary $\partial\Omega$ by the diffusing species (see Anand et al., 2019). Denoting ψ as the free energy per unit reference volume, this constraint takes the form of the following free energy imbalance,

$$\frac{\mathrm{d}}{\mathrm{d}t} \int_{\Omega} \psi \, \mathrm{d}V \leq \int_{\partial\Omega} \dot{W}_e \, \mathrm{d}S + \int_{\partial\Omega} \mu \, \mathbf{J} \cdot \mathbf{n} \, \mathrm{d}S . \tag{9}$$

Consider now the local balance equations and recall that the external work is given by the right-hand side of (5). Applying the divergence theorem to the last term in (9), considering the strain partitioning (2) and replacing virtual fields (δa) by realisable velocity fields ($\dot{a}$), one reaches:

$$\int_{\Omega} \left[\dot{\psi} - \left(\boldsymbol{\sigma} : \dot{\boldsymbol{\varepsilon}}^e + \boldsymbol{q} : \dot{\boldsymbol{\varepsilon}}^p + \omega\dot{\phi} + \boldsymbol{\xi} \cdot \nabla\dot{\phi} \right) + \mu\dot{C} - \mathbf{J} \cdot \nabla\mu \right] \mathrm{d}V \leq 0, \tag{10}$$

where a plastic micro-stress tensor $\boldsymbol{q}$ has been defined (work-conjugate to $\boldsymbol{\varepsilon}^p$). Since (10) must hold for any volume Ω, it follows that it must also hold in a local fashion, such that the local free-energy imbalance reads,

$$\dot{\psi} - \boldsymbol{\sigma} : \dot{\boldsymbol{\varepsilon}} - \omega\dot{\phi} - \boldsymbol{\xi} \cdot \nabla\dot{\phi} + \mu\dot{C} - \mathbf{J} \cdot \nabla\mu \leq 0 . \tag{11}$$

Accordingly, appropriate constitutive relations must be considered in order to fulfil the following imbalance:

$$\left(\boldsymbol{\sigma} - \frac{\partial\psi}{\partial\boldsymbol{\varepsilon}^e} \right) : \dot{\boldsymbol{\varepsilon}}^e + \left(\boldsymbol{q} - \frac{\partial\psi}{\partial\boldsymbol{\varepsilon}^p} \right) : \dot{\boldsymbol{\varepsilon}}^p + \left(\omega - \frac{\partial\psi}{\partial\phi} \right) \dot{\phi} + \left(\boldsymbol{\xi} - \frac{\partial\psi}{\partial\nabla\phi} \right) \cdot \nabla\dot{\phi}$$
$$- \left[\left(\mu - \frac{\partial\psi}{\partial C} \right) \dot{C} - \mathbf{J} \cdot \nabla\mu \right] \geq 0, \tag{12}$$

2.4. Constitutive theory

We shall now proceed to develop a constitutive theory for the coupled deformation-diffusion-fracture problem that is consistent with the free energy imbalance, Eq. (12).

10

2.4.1. Mechanism-based elasto-plasticity

We start by outlining the constitutive choices that characterise the microstructural changes leading to plasticity and fracture. First, the influence of damage into the mechanical deformation of the body is captured by defining a deformation free energy that decreases with the phase field variable ϕ. Specifically, the following quadratic degradation function is chosen:

$$g\left(\phi\right) = \left(1 - \phi\right)^2 . \tag{13}$$

Thus, the relation between the Cauchy stress tensor $\boldsymbol{\sigma}$ and the undamaged stress tensor $\boldsymbol{\sigma}_0$ follows immediately. Omitting the negligible role of lattice dilation (Hirth, 1980) and consistent with (12), the stress tensor is given by

$$\boldsymbol{\sigma} = \frac{\partial \psi}{\partial \boldsymbol{\varepsilon}^e} = \left(1 - \phi\right)^2 \boldsymbol{\sigma}_0 = \left(1 - \phi\right)^2 \boldsymbol{C}^e : \boldsymbol{\varepsilon}^e = \left(1 - \phi\right)^2 \boldsymbol{C} : \boldsymbol{\varepsilon} , \tag{14}$$

where $\boldsymbol{C}^e$ denotes the elastic stiffness tensor and $\boldsymbol{C}$ is the consistent elastic-plastic material Jacobian. As discussed in the introduction, the latter is defined in a suitable manner to capture the important role that dislocation hardening mechanisms associated with GNDs and plastic strain gradients play on crack tip mechanics. For this, a mechanism-based formulation is developed, grounded on Taylor (1938) dislocation model (Huang et al., 2004; Liu et al., 2005).

Considering Taylor (1938) model as underlying principle, the shear flow stress τ is formulated in terms of the dislocation density ρ as

$$\tau = \alpha G b \sqrt{\rho} , \tag{15}$$

where α is an empirical coefficient taking values between 0.3 and 0.5, G denotes the shear modulus, and b corresponds to the Burger's vector. The

dislocation density can be additively decomposed into the sum of the density of statistically stored dislocations (SSDs) ρ_S, which trap each other in a random way, and the density of geometrically necessary dislocations (GNDs) ρ_G, which are required for the compatible deformation of the crystal. Hence,

$$\rho = \rho_S + \rho_G \,. \tag{16}$$

The GND density ρ_G is related to the effective plastic strain gradient η^p by:

$$\rho_G = \bar{r} \frac{\eta^p}{b} \,, \tag{17}$$

where $\bar{r}$ is the Nye-factor, which is assumed to be approximately 1.90 (Arsenlis and Parks, 1999; Shi et al., 2004). Following Fleck and Hutchinson (1997), three quadratic invariants of the plastic strain gradient tensor are used to represent the effective plastic strain gradient η^p as

$$\eta^p = \left(c_1 \eta^p_{iik} \eta^p_{jjk} + c_2 \eta^p_{ijk} \eta^p_{ijk} + c_3 \eta^p_{ijk} \eta^p_{kji} \right)^{1/2} \,. \tag{18}$$

The coefficients have been determined to be equal to $c_1 = 0$, $c_2 = 1/4$ and $c_3 = 0$ from three dislocation models for bending, torsion and void growth (Gao et al., 1999), leading to

$$\eta^p = \frac{1}{2} \left(\boldsymbol{\eta}^p \boldsymbol{\eta}^p \right)^{1/2} \,, \tag{19}$$

where the components of the strain gradient tensor are obtained by $\eta^p_{ijk} = \varepsilon^p_{ik,j} + \varepsilon^p_{jk,i} - \varepsilon^p_{ij,k}$. The tensile flow stress σ_f is related to the shear flow stress τ through the Taylor factor M, such that

$$\sigma_f = M\tau = M\alpha Gb\sqrt{\rho} \,. \tag{20}$$

12

This linear dependence of the square of plastic flow stress on strain gradients, resulting from Taylor (1938) dislocation model, is intrinsic to the mechanism-based strain gradient (MSG) plasticity theory and is grounded on the nano-indentation experiments by Nix and Gao (1998). Rearranging Eqs. (15-17) and substituting into (20), the flow stress can be re-formulated as

$$\sigma_f = M\alpha Gb\sqrt{\rho_S + \bar{r}\frac{\eta^p}{b}}\,.\tag{21}$$

The SSD density ρ_S can be determined from (21) knowing the relation in uniaxial tension between the flow stress and the material stress-strain curve as follows

$$\rho_S = \left(\frac{\sigma_{ref}f(\varepsilon^p)}{M\alpha Gb}\right)^2\tag{22}$$

Here, σ_{ref} is a reference stress and f is a non-dimensional function of the equivalent plastic strain ε^p, as given from the uniaxial stress-strain curve. Substituting back into (21), σ_f yields:

$$\sigma_f = \sigma_{ref}\sqrt{f^2(\varepsilon^p) + L_p\eta^p}\tag{23}$$

where L_p is the intrinsic plastic material length. It can be readily seen that conventional von Mises plasticity is recovered if $L_p = 0$ or if the gradient-related term $L_p\eta^p$ becomes negligible relative to the characteristic length of plastic deformation. Also, we emphasise that the theory is intended to model a collective behaviour of dislocations, implying that it is only applicable at a much larger scale than the average dislocation spacing; i.e. distances of 100 nm or larger. This is also the scale over which the differences between higher order and lower order versions of mechanism-based strain gradient plasticity are relevant (Shi et al., 2001). I.e., identical results are expected

13

over the regime where continuum models are applicable - a distance of 100 nm or larger ahead of the crack tip. Thus, we choose to adopt a lower order formulation by using a viscoplastic approach, following Huang et al. (2004). The purpose is to overcome the need for higher order stresses by constructing a self-contained model through the viscoplastic relation between $\dot{\varepsilon}^p$ and the effective von Mises stress σ_e. To mimic a rate-independent response, we use the viscoplastic-limit approach by Kok et al. (2002), which entails replacing the reference strain rate $\dot{\varepsilon}_0$ with the effective strain rate $\dot{\varepsilon}$. Accordingly, the effective plastic strain rate is defined as,

$$\dot{\varepsilon}^p = \dot{\varepsilon} \left[\frac{\sigma_e}{\sigma_{ref} \sqrt{f^2 \left(\varepsilon^p \right) + L_p \eta^p}} \right]^m , \tag{24}$$

where m is the strain rate sensitivity exponent; values larger than 5 provide a response similar to that of rate-independent solids, with no differences being observed for $m \geq 20$ (Huang et al., 2004). A value of $m = 20$ is adopted in this work. The consistent material Jacobian is then given by (Martínez-Pañeda et al., 2017; Qu et al., 2004),

$$\boldsymbol{\sigma}_0 = K \mathrm{tr} \left(\dot{\boldsymbol{\varepsilon}} \right) \boldsymbol{\delta} + 2\mu \left\{ \dot{\boldsymbol{\varepsilon}}' - \frac{3\dot{\varepsilon}}{2\sigma_e} \left[\frac{\sigma_e}{\sigma_{ref} \sqrt{f^2 \left(\varepsilon^p \right) + L_p \eta^p}} \right]^m \right\}. \tag{25}$$

Here, K is the bulk modulus and $\boldsymbol{\delta}$ is the Kronecker delta. Finally, the plastic hardening behaviour is given by the following isotropic hardening power law:

$$\sigma = \sigma_Y \left(1 + \frac{E \varepsilon^p}{\sigma_Y} \right)^N \tag{26}$$

where N is the strain hardening exponent ($0 \leq N \leq 1$). Accordingly, $\sigma_{ref} = \sigma_Y (E/\sigma_Y)^N$ and $f(\varepsilon^p) = (\varepsilon^p + \sigma_Y/E)^N$. The mechanical constitutive response of the solid is then completely characterised by the damage

14

degradation function (13), the Cauchy stress definition (14) and the consistent material Jacobian (25).

2.4.2. Hydrogen-sensitive phase field damage

We proceed to describe the fracturing process by following and extending the phase field model for hydrogen embrittlement developed by Martínez-Pañeda et al. (2018). The idea is to approximate the fracture energy density ψ^f over a discontinuous surface Γ by using a smooth and continuous auxiliary (phase) field that smears the crack. The model is non-local and involves as a consequence a phase field length scale ℓ, which governs the smearing of the crack. It has been shown using Gamma-convergence that the regularised fracture energy converges to the original form for a vanishing value of ℓ (Bellettini and Coscia, 1994; Chambolle, 2004). Accordingly, for a material of toughness G_c,

$$\psi^f = \int_\Gamma G_c \, \mathrm{d}S \approx \int_\Omega G_c \gamma\left(\phi, \nabla\phi\right) \, \mathrm{d}V \,. \tag{27}$$

Here, γ is the crack density functional, which is here chosen to be:

$$\gamma\left(\phi, \nabla\phi\right) = \frac{\phi^2}{2\ell} + \frac{\ell}{2}|\nabla\phi|^2 \,. \tag{28}$$

This phase field approximation circumvents the need to track discrete crack surfaces, enabling the modelling of complex fracture phenomena (see, e.g., McAuliffe and Waisman, 2015; Hirshikesh et al., 2019; Quintanas-Corominas et al., 2020).

Hydrogen comes into the picture by degrading the toughness of the solid, as consistently observed in laboratory experiments (Gangloff, 2003). The

specific degradation law can be chosen in a phenomenological manner or by establishing a connection with the underlying physical micromechanisms. Both options will be explored here. In its most general form, the evolution of the critical fracture energy can be given by,

$$G_c(C) = f(C) G_c(0),$$ (29)

where $f(C)$ is a hydrogen degradation function. In this work, the focus will be on alloys that exhibit intergranular fracture in the presence of hydrogen. Thus, we enrich (29) by defining $f(C)$ to be a function of the hydrogen trapped at the grain boundaries, as predicted by the multi-trap hydrogen transport model described below.

It remains to define the constitutive relations for the micro-stress variables work conjugate to the phase field and the phase field gradient. Denoting by ψ^b the bulk strain energy density of the solid, the scalar micro-stress ω is given by,

$$\omega = \frac{\partial \psi}{\partial \phi} = -2(1 - \phi)\psi^b + G_c(C)\frac{\phi}{\ell}.$$ (30)

Likewise, the phase field micro-stress vector $\boldsymbol{\xi}$ reads:

$$\boldsymbol{\xi} = \frac{\partial \psi}{\partial \nabla \phi} = G_c(C)\, \ell\, \nabla \phi.$$ (31)

Accordingly, the phase field local balance (6c) can be re-formulated by considering the constitutive choices (30) and (31). Assuming a zero concentration gradient along the small region where $\nabla \phi \neq 0$, the phase field evolution equation reads:

$$G_c(C) \left(\frac{\phi}{\ell} - \ell \nabla^2 \phi \right) - 2(1 - \phi)\psi^b = 0.$$ (32)

16

Fracture is assumed to be driven by the bulk strain energy density of the solid, which is here defined as the summation of the elastic and plastic strain energy densities:

$$\psi^b = \psi^e + \psi^p = \frac{1}{2}\boldsymbol{\varepsilon}^e : \boldsymbol{C}^e : \boldsymbol{\varepsilon}^e + \int_0^t (\boldsymbol{\sigma} : \dot{\boldsymbol{\varepsilon}}^p) \, \mathrm{d}t \,. \tag{33}$$

where $\boldsymbol{C}^e$ is the linear elastic stiffness matrix. Thus, both elastic and plastic strain energy densities contribute on an equal footing to the fracture process, as in e.g. (Miehe et al., 2016; Martínez-Pañeda et al., 2020b). Other approaches have also been proposed, including a driving force for fracture based purely on the elastic stored energy (Duda et al., 2015, 2018) or the consideration of elastic and plastic energies with a different weighting (see, e.g., Borden et al., 2016; You et al., 2021). A physically-sound choice is not straightforward as it is unclear to what extent a Griffith-type energy balance applies to ductile fracture (Hutchinson, 1983; Orowan, 1948).

2.4.3. A multi-trap model for hydrogen transport

Our theory deals with the dilute transport of hydrogen in metals. Hydrogen atoms occupy normal interstitial lattice sites (NILS) and can additionally reside at trapping sites such as interfaces or dislocations. We adopt the common assumptions of the literature (see, e.g., Di Leo and Anand, 2013; Sofronis and McMeeking, 1989) and base our modelling on the equilibrium theory presented by Oriani (Oriani and Josephic, 1974). The subscript L refers to lattice sites and the subscript T to trap sites. Superscripts are used to denote the different trap sites. It is assumed that traps are isolated (i.e., do not form an extended network). Hence, hydrogen transport between trap sites is by lattice diffusion.

The hydrogen concentration in lattice sites is given by,

$$C_L = N_L \beta \, \theta_L \tag{34}$$

where N_L is the density of the host metal lattice measured in solvent atoms per unit volume, β is the number of interstitial sites per atom, and θ_L is the lattice occupancy fraction ($0 \leq \theta_L \leq 1$). The number of interstitial sites per solvent atom β is typically taken to be equal to 6 for bcc metals, as indirect evidence suggests that tetrahedral site occupancy is favoured relative to octahedral site occupancy at room temperature (Hirth, 1980; Kiuchi and McLellan, 1983). For fcc lattices, $\beta = 1$ is usually assumed, resulting from the more favourable octahedral site occupancy. The density of solvent atoms is a function of the molar volume of the host lattice V_M and Avogadro's number N_A as,

$$N_L = \frac{N_A}{V_M} = \frac{N_A \rho_M}{M_M}, \tag{35}$$

where ρ_M is the density and M_M is the molar mass. In the case of iron at 293 K, the density equals $\rho_M = 7.87 \times 10^3$ kg/m^3 and the atomic weight $M_M = 55.8 \times 10^{-3}$ kg/mol; this implies $N_L = 8.46 \times 10^{28}$ sites/m^3.

Hydrogen can also be retained at so-call hydrogen *traps*. These are typically microstructural defects such as dislocations, grain boundaries, voids, carbides and interfaces. These traps can be reversible or irreversible, and can also be classified as saturable or unsaturable. Reversible traps are those that can immobilize and release hydrogen while irreversible traps are those that absorb hydrogen and prevent it from escaping. However, one should

note that the term irreversible is not fundamentally correct but rather pragmatic, as leakage can always take place for a sufficiently long timescale or a sufficiently high temperature (Turnbull, 2015). Multiple trap types are considered here - the hydrogen concentration in the ith type of trapping site can be defined as:

$$C_T^{(i)} = \theta_T^{(i)} \alpha^{(i)} N_T^{(i)} \tag{36}$$

where N_T is the trap density, α is the number of atom sites per trap and θ_T is the fraction of occupied trapping sites. Hence, αN_T is the number of trapping sites per unit volume. We choose to adopt $\alpha = 1$ and use apparent binding energies. The total hydrogen concentration is, therefore, the sum of the lattice hydrogen concentration and the concentration at each of the trap types considered:

$$C = C_L + \sum_i^n C_T^{(i)} . \tag{37}$$

where n is the total number of trap types.

The relation between the lattice and trapped hydrogen concentrations is assumed here following Oriani's equilibrium theory (Oriani and Josephic, 1974). Thus, there is a Fermi-Dirac relation between the occupancy of the ith type of trapping sites and the fraction of occupied lattice sites

$$\frac{\theta_T^{(i)}}{1 - \theta_T^{(i)}} = \frac{\theta_L}{1 - \theta_L} K^{(i)} , \tag{38}$$

with $K^{(i)}$ being the equilibrium constant for the ith type of trap, given by

$$K^{(i)} = \exp\left(\frac{-W_B^{(i)}}{RT}\right) . \tag{39}$$

19

Here, R is the gas constant, T is the absolute temperature, and W_B is the binding energy - an inherently negative quantity that quantifies the energy required for a hydrogen atom to escape a trap site and move into a lattice site. In many alloys, especially in bcc lattices, conditions of low occupancy $\theta_L << 1$ are usually assumed, such that

$$\frac{\theta_L}{1 - \theta_L} \approx \theta_L \tag{40}$$

Considering (34), (36) and (38), then the relation between the lattice and trapped concentration is established as,

$$C_T^{(i)} = \frac{K^{(i)} \alpha^{(i)} N_T^{(i)}}{\beta N_L + \left(K^{(i)} - 1\right) C_L} C_L \tag{41}$$

Mass diffusion is driven by gradients of chemical potential $\nabla \mu$. The mass flux is related to $\nabla \mu$ through a linear Onsager relation, grounded on Einstein's equation of diffusion. Accordingly, for a material with a diffusion coefficient D, the flux reads

$$\mathbf{J} = -\frac{D}{RT} C_L \nabla \mu \,. \tag{42}$$

Thus, hydrogen atoms migrate from regions of high chemical potential to regions of low chemical potential. Note that, for simplicity, the L subscript is omitted from $\mathbf{J}$ and μ but both are related to the transport of hydrogen between interstitial lattice sites. The chemical potential is defined as,

$$\mu = \mu^0 + RT \ln\frac{\theta_L}{1 - \theta_L} - \bar{V}_H \sigma_H \,, \tag{43}$$

where μ^0 denotes the chemical potential in the standard state, σ_H is the hydrostatic stress, and $\bar{V}_H$ is the partial molar volume of hydrogen in solid

solution ($\bar{V}_H = 2000$ mm^3/mol for iron-based materials). As evident from (43), the role of hydrostatic tensile stresses (volumetric strains) is to lower the chemical potential, increasing the hydrogen solubility in the lattice as a result of lattice dilatation.

Substituting (43) into (42) and adopting the common approximation of a constant interstitial sites concentration ($\nabla N_L = 0$) gives:

$$\mathbf{J} = -D\nabla C_L + \frac{D}{RT}C_L\bar{V}_H\nabla\sigma_H \tag{44}$$

Fluxes, due to the chemical potential gradient, and hydrogen concentrations are related through the requirement of mass conservation:

$$\frac{\mathrm{d}}{\mathrm{d}t}\int_V C \, \mathrm{d}V + \int_S \mathbf{J}\cdot\mathbf{n} \, \mathrm{d}S = 0 \tag{45}$$

Exploiting Oriani's equilibrium, an effective diffusion coefficient D_e can be defined for a multi-trap system, such that the D/D_e ratio reads,

$$\frac{D}{D_e} = 1 + \sum_i \frac{\partial C_T^{(i)}}{\partial C_L} = 1 + \sum_i \left(\frac{K^{(i)}\alpha^{(i)}N_T^{(i)}/(\beta N_L)}{[1 + (K^{(i)}-1)\,C_L/(\beta N_L)]^2} \right) \tag{46}$$

Now, consider Eqs. (37), and (44)-(46). Making use of the divergence theorem and noting that (45) must hold for any arbitrary volume, the local mass balance can be derived as,

$$\frac{D}{D_e}\frac{\partial C_L}{\partial t} = D\nabla^2 C_L - \nabla\left(\frac{DC_L}{RT}\bar{V}_H\nabla\sigma_H\right). \tag{47}$$

It remains to define a constitutive choice for the trap density $N_T^{(i)}$. The trap density is often a material property that remains constant throughout the analysis, as it is the case for traps such as carbides or grain boundaries. However, dislocation traps evolve with mechanical loading and thus a

constitutive law must be defined for $N_T^{(d)}$. We build upon the Taylor-based formulation presented above to establish an evolution law for $N_T^{(d)}$ in terms of the total dislocation density ρ, including both contributions from SSDs and GNDs. By assuming one trap site per atomic plane threaded by a dislocation, the following relation between the dislocation density ρ and the trap site density $N_T^{(d)}$ can be identified:

$$N_T^{(d)} = \frac{1}{b}\rho \tag{48}$$

where the pre-factor is the inverse of the Burgers vector, as slip occurs along the plane of the shortest Burgers vector. The total dislocation density can be computed from Eqs. (16), (17) and (22). Denoting a the lattice parameter, the Burgers vector is given by $b = \sqrt{2}/a = 0.2555$ nm for fcc metals, as slip occurs along the closed packed plane 111 and slip direction $\langle\bar{1}10\rangle$. For bcc metals $b = 2/(\sqrt{3}a) = 0.2725$ nm, as slip is assumed to occur along the $\{110\}$ plane and $\langle111\rangle$ direction. The reader is referred to, e.g., (Davey, 1925) for a list of lattice constants for various metals.

3. Numerical implementation

We shall now describe the numerical implementation of our coupled theory, in the context of the finite element method. First, the elastic strain energy density is decomposed to prevent the evolution of damage under compressive loading (Section 3.1). Secondly, in Section 3.2, a history field is defined to prevent phase field damage reversibility. Finally, in Section 3.3, we address the discretisation of the weak formulation of our theory and formulate the residuals and the stiffness matrices. The implementation is conducted

22

within an Abaqus user-element (UEL) subroutine, with the pre-processing of the input files carried out using Abaqus2Matlab (Papazafeiropoulos et al., 2017).

3.1. Addressing damage in compression and crack interpenetration

Several formulations have been proposed to effectively decompose the elastic fracture driving force into tension and compression components, so as to prevent the nucleation of cracks under compressive stresses. Here, we follow the spherical/deviatoric split proposed by Amor et al. (2009). Thus, in a solid with Lame's first parameter λ, the elastic strain energy density can be decomposed as $\psi^e = \psi^e_+ + \psi^e_-$, with

$$
\begin{aligned}
\psi^e_+ &= \frac{1}{2}\left(\lambda + \frac{2}{3}G\right)\langle \operatorname{tr} \boldsymbol{\varepsilon}^e \rangle^2_+ + G\,|\boldsymbol{\varepsilon}^{e'}|^2 \\
\psi^e_- &= \frac{1}{2}\left(\lambda + \frac{2}{3}G\right)\langle \operatorname{tr} \boldsymbol{\varepsilon}^e \rangle^2_- \,,
\end{aligned}
\tag{49}
$$

and only ψ^e_+ contributing to damage. Here, $\langle\rangle$ denotes the Macaulay brackets. The strain energy decomposition is implemented by means of a hybrid approach, following Ambati et al. (2015). This implies that the split of the elastic strain energy density is incorporated into the phase field force balance but not considered in the balance of linear momentum. In addition, crack interpenetration is prevented by adding the following constraint (Ambati et al., 2015)

$$
\phi = 0 \qquad \text{if } \psi^e_+ < \psi^e_-.
\tag{50}
$$

3.2. Damage irreversibility

Additional numerical restrictions are needed to ensure damage irreversibility, Eq. (3). These constraints are restricted to the evolution of the elastic

23

strain energy density, as it is assumed that the effective plastic work is monotonically increasing. We follow Miehe et al. (2010) and introduce a history variable field $\mathcal{H}$. To ensure irreversible growth of the phase field variable, the history field must satisfy the Kuhn-Tucker conditions:

$$\psi_+^e - \mathcal{H} \leq 0\,, \quad \dot{\mathcal{H}} \leq 0\,, \quad \dot{\mathcal{H}}\left(\psi_+^e - \mathcal{H}\right) = 0 \tag{51}$$

Thus, for a total time t_t, the history variable at time t corresponds to the maximum value of ψ_+^e, i.e.:

$$\mathcal{H} = \max_{t \in [0, t_t]} \psi_+^e(t). \tag{52}$$

3.3. Finite element discretisation

We proceed now to describe the finite element discretisation and the formulation of the residuals and stiffness matrices. Our numerical implementation uses as nodal unknowns the following fields: displacement $\mathbf{u}$, phase field ϕ, and lattice hydrogen concentration C_L. We derive the weak form of the balance equation for each of these fields considering the constitutive choices outlined in Section 2. Neither body forces nor external tractions are considered, for simplicity. Thus, recalling (5) and (13), the weak form for the mechanical problem reads,

$$\int_\Omega \left\{ \left[(1 - \phi)^2 + k\right] \boldsymbol{\sigma}_0 : \delta\boldsymbol{\varepsilon} \right\} \mathrm{d}V = 0\,. \tag{53}$$

where k is a small positive-valued constant that is introduced to prevent ill-conditioning when $\phi = 1$; a value of $k = 1 \times 10^{-7}$ is chosen throughout this study. Regarding the phase field, the weak form is derived upon considering the history field $\mathcal{H}$ described above and combining (5) and (32), rendering:

$$\int_\Omega \left[-2(1 - \phi)\delta\phi\,\mathcal{H} + G_c\left(C\right)\left(\frac{\phi}{\ell}\delta\phi + \ell\nabla\phi \cdot \nabla\delta\phi\right) \right] \mathrm{d}V = 0\,. \tag{54}$$

24

Finally, the weak form for the hydrogen transport problem can be readily obtained by multiplying Eq. (47) by a test function δC_L and integrating over the problem domain, such that:

$$\int_{\Omega} \left[\delta C_L \left(\frac{1}{D_e} \frac{dC_L}{dt} \right) + \nabla \delta C_L \nabla C_L - \nabla \delta C_L \left(\frac{\bar{V}_H C_L}{RT} \nabla \sigma_H \right) \right] \mathrm{d}V = 0 \,. \quad (55)$$

Now make use of Voigt notation. The nodal variables for the displacement field $\hat{\mathbf{u}}$, the phase field $\hat{\phi}$ and the lattice hydrogen concentration $\hat{C}_L$ are interpolated as:

$$\mathbf{u} = \sum_{i=1}^{m} \boldsymbol{N}_i \hat{\mathbf{u}}_i, \qquad \phi = \sum_{i=1}^{m} N_i \hat{\phi}_i, \qquad C_L = \sum_{i=1}^{m} N_i \hat{C}_{L_i}. \quad (56)$$

Here, N_i denotes the shape function associated with node i and $\boldsymbol{N}_i$ is the shape function matrix, a diagonal matrix with N_i in the diagonal terms. Also, m is the total number of nodes per element such that, assuming plane strain conditions, $\hat{\mathbf{u}}_i = \{u_x, \, u_y\}^T$, $\hat{\phi}_i$ and $\hat{C}_{L_i}$ respectively denote the displacement, phase field and lattice hydrogen concentration at node i. Consequently, the associated gradient quantities can be discretised using the corresponding **B**-matrices, containing the derivative of the shape functions, such that:

$$\boldsymbol{\varepsilon} = \sum_{i=1}^{m} \boldsymbol{B}_i^{\boldsymbol{u}} \hat{\mathbf{u}}_i, \qquad \nabla \phi = \sum_{i=1}^{m} \mathbf{B}_i \hat{\phi}_i, \qquad \nabla C_L = \sum_{i=1}^{m} \mathbf{B}_i \hat{C}_{L_i} \,. \quad (57)$$

Considering the discretisation (56)-(57), we derive the residuals for each primal kinematic variable as:

$$\mathbf{R}_i^{\mathbf{u}} = \int_{\Omega} \left\{ \left[(1 - \phi)^2 + k \right] (\boldsymbol{B}_i^{\mathbf{u}})^T \boldsymbol{\sigma}_0 \right\} \mathrm{d}V \,, \quad (58)$$

$$R_i^{\phi} = \int_{\Omega} \left\{ -2 \left(1 - \phi \right) N_i \mathcal{H} + G_c(C) \left[\frac{\phi}{\ell} N_i + \ell \, (\mathbf{B}_i)^T \nabla \phi \right] \right\} dV \,, \quad (59)$$

$$R_i^{C_L} = \int_{\Omega} \left[N_i \left(\frac{1}{D_e} \frac{\mathrm{d}C_L}{\mathrm{d}t} \right) + \mathbf{B}_i^T \nabla C_L - \mathbf{B}_i^T \left(\frac{\overline{V}_H C_L}{RT} \nabla \sigma_H \right) \right] \mathrm{d}V \,. \quad (60)$$

25

The consistent tangent stiffness matrices $\boldsymbol{K}$, required to complete the finite element implementation, are obtained by considering the constitutive relations and differentiating the residuals with respect to the incremental nodal variables as follows:

$$\boldsymbol{K}_{ij}^{\mathbf{u}} = \frac{\partial \boldsymbol{R}_i^{\boldsymbol{u}}}{\partial \boldsymbol{u}_j} = \int_\Omega \left\{ \left[(1-\phi)^2 + k \right] (\boldsymbol{B}_i^{\boldsymbol{u}})^T \boldsymbol{C} \, \boldsymbol{B}_j^{\boldsymbol{u}} \right\} \, \mathrm{d}V \,, \tag{61}$$

$$\boldsymbol{K}_{ij}^{\phi} = \frac{\partial R_i^{\phi}}{\partial \phi_j} = \int_\Omega \left\{ \left(2\mathcal{H} + \frac{G_c\left(C\right)}{\ell} \right) N_i N_j + G_c\left(C\right) \ell \, \mathbf{B}_i^T \mathbf{B}_j \right\} \, \mathrm{d}V \,, \tag{62}$$

$$\boldsymbol{K}_{ij}^{C_L} = \frac{\partial R_i^{C_L}}{\partial c_j} = \int_\Omega \left(N_i^T \frac{1}{D_e \mathrm{d}t} N_j + \mathbf{B}_i^T \mathbf{B}_j - \mathbf{B}_i^T \frac{\overline{V}_H}{RT} \nabla \sigma_H N_j \right) \, \mathrm{d}V \,. \tag{63}$$

The Newton-Raphson method is used to iteratively solve the global finite element system. A so-called staggered or alternative minimisation solution scheme is used, following (Miehe et al., 2010; Martínez-Pañeda et al., 2018). A time sensitivity study is conducted in all computations.

4. Results

We proceed to demonstrate the potential of the theoretical and computational framework presented by simulating several boundary value problems of particular interest. First, in Section 4.1, the boundary layer concept is exploited to demonstrate that the model can capture the main experimental trends and to gain insight into the interplay between hydrogen and dislocation-hardening mechanisms. Then, in Section 4.2, model predictions are benchmarked against experiments conducted on AISI 4135 steel.

4.1. Crack tip mechanics and growth resistance

We shall first investigate the mechanics of stationary and propagating cracks by considering the fracture of a metallic sample under small scale

yielding conditions. The concept of a boundary layer formulation is illustrated in Fig. 1, using as example a Compact Tension specimen. For a cracked solid, the crack tip stress state is characterised by the stress intensity factor; K_I, assuming mode I conditions. The Williams (1957) solution for a linear elastic solid can be used to relate the displacement field to the magnitude of K_I. Considering a polar coordinate system (r, θ) and a Cartesian coordinate system (x, y) centred at the crack tip, with the crack plane along the negative x-axis, the displacement solution reads:

$$u_i = \frac{K_I}{E} r^{1/2} f_i (\theta, \nu),$$ (64)

where the subscript index i equals x or y, and the functions $f_i (\theta, \nu)$ are given by

$$f_x = \frac{1 + \nu}{\sqrt{2\pi}} (3 - 4\nu - \cos \theta) \cos \left(\frac{\theta}{2} \right)$$ (65)

$$f_y = \frac{1 + \nu}{\sqrt{2\pi}} (3 - 4\nu - \cos \theta) \sin \left(\frac{\theta}{2} \right).$$ (66)

After a mesh-sensitivity analysis, the finite element model is discretised with approximately 24,000 quadratic, quadrilateral elements with reduced integration. The mesh is uniformly refined in the vicinity of the crack and the region of crack extension, such that the fracture process is resolved by ensuring that the characteristic element length is at least 6 times smaller than the phase field length scale. In this boundary value problem, the results obtained are independent from the size of the crack and the radius of the specimen, as long as these two dimensions are significantly larger than the plastic zone size, R_p.
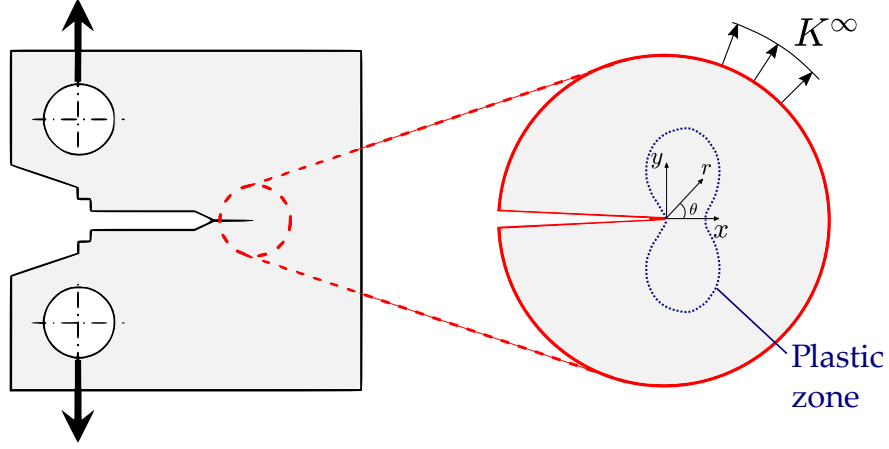
Figure 1: Boundary layer concept under small scale yielding conditions, illustrated on a Compact Tension specimen.

We simulate crack initiation and growth in a model steel with Young's modulus $E = 200$ GPa, Poisson's ratio $\nu = 0.3$, yield stress $\sigma_Y = 600$ MPa, and strain hardening exponent $N = 0.2$. Regarding the mass diffusion properties, a lattice diffusion coefficient of $D = 0.0127$ mm^2/s is adopted, following Sofronis and McMeeking (1989). We consider the existence of three types of traps: dislocations, carbides and grain boundaries. The dislocation trap density $N_T^{(d)}$ is given by Eq. (48) and the binding energy is assumed to be $W_B^{(d)} = -20.2$ kJ/mol (Hirth, 1980). Carbide trap sites are characterised by a trap density of $\alpha N_T^{(c)} = 8.464 \times 10^{17}$ sites/mm^3 (Li et al., 2004) and a binding energy of $W_B^{(c)} = -11.5$ kJ/mol (Dadfarnia et al., 2011). Lastly, the trapping characteristics of grain boundaries are given by $W_B^{(gb)} = -30$ kJ/mol (Serebrinsky et al., 2004) and $\alpha N_T^{(gb)} = 8.464 \times 10^{13}$ sites/mm^3 (Dadfarnia et al., 2011).

28

To facilitate interpretation of the crack growth resistance results, we shall first investigate the behaviour of a stationary crack; i.e., disregarding the damage part of the formulation. Crack tip fields are shown normalising the distance ahead of the crack r with Irwin's estimate of the plastic zone size:

$$R_p = \frac{1}{3\pi} \left(\frac{K_I}{\sigma_Y} \right)^2 . \tag{67}$$

The distribution of the tensile stress component σ_{yy} is shown in Fig. 2a for both the cases of $L_p = 0.03R_p$ and $L_p = 0$ (conventional plasticity). It is observed that dislocation hardening mechanisms associated with plastic strain gradients are negligible far away from the crack tip but become significant within a distance of $r/R_p = 0.01$. The GND densities resulting from the large gradients of plastic strain present near the crack tip result in stress levels that are significantly larger than those predicted by conventional plasticity models ($L_p = 0$). This is in agreement with expectations (Martínez-Pañeda and Fleck, 2019). The hydrostatic stress distribution shows similar differences between gradient-enriched and conventional plasticity predictions and this leads, in turn, to a larger hydrogen concentration. The lattice hydrogen concentration ahead of the crack tip is shown in Fig. 2b. The results have been obtained with a loading rate of $\dot{K}_I = 0.183$ MPa$\sqrt{\text{m}}$/s and by defining an initial hydrogen concentration of $C_0 = 0.1$ wt ppm. The higher lattice hydrogen concentration predicted in the case of $L_p > 0$ is not surprising given the dependence of the lattice hydrogen concentration on the hydrostatic stress; under steady state conditions, their relation reads:

$$C_L = C_0 \exp \left(\frac{\bar{V}_H \sigma_H}{RT} \right) . \tag{68}$$

Thus, small changes in the hydrostatic stress distribution can lead to signif-

29

icant differences in the lattice hydrogen concentration.

(a)

(b)
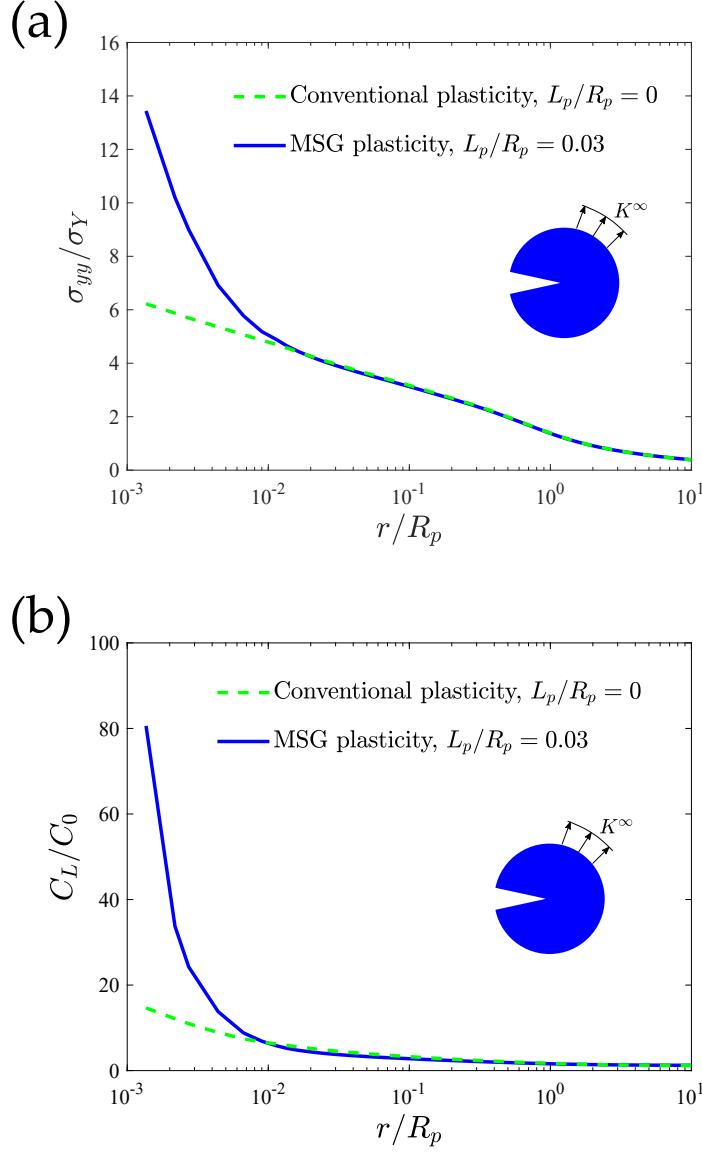

Figure 2: Stationary crack tip analysis: (a) tensile stress and (b) lattice hydrogen concentration distributions ahead of the crack $(r, \theta = 0°)$. Results are shown for both mechanism-based strain gradient (MSG) plasticity $(L_p/R_p = 0.03)$ and conventional plasticity $(L_p/R_p = 0)$.

Moreover, the enriched crack tip mechanics description provided by the model captures another interesting effect. While local hardening due to strain gradients increases crack tip stresses and reduces the degree of plastic dissipation, this does not necessarily translate into a smaller crack tip dislocation density. The density of Statistically Stored Dislocations (SSDs) ρ_S diminishes with increasing L_p/R_p but this is counteracted by the associated increase in the density of Geometrically Necessary Dislocations (GNDs) ρ_G. The distributions of ρ_G and ρ_S are shown in Fig. 3. It can be observed that, for the choice $L_p/R_p = 0.03$, the density of GNDs ρ_G becomes larger than the density of SSDs ρ_S close to the crack tip. This elevates the total density close to the crack tip, which has implications for the hydrogen trapped in dislocations.
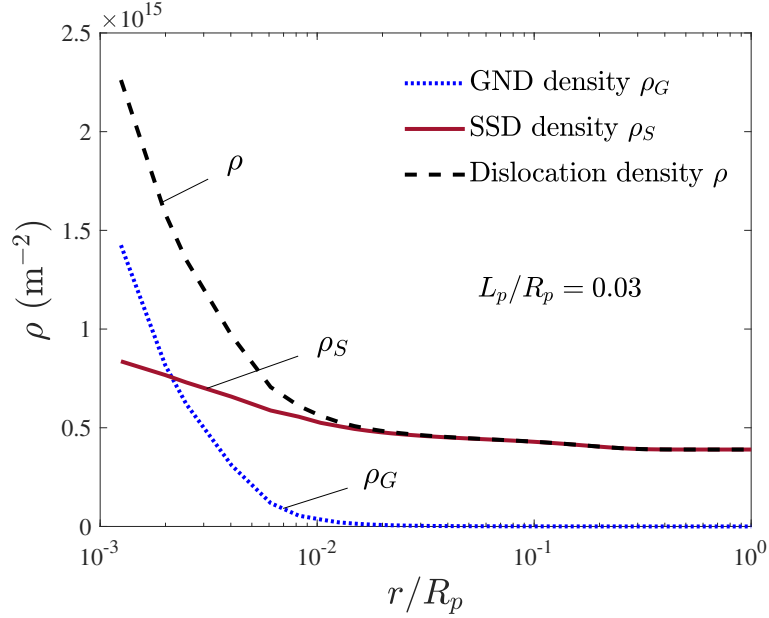
Figure 3: Stationary crack tip analysis: dislocation density distribution (in m^{-2}) ahead of the crack $(r, \theta = 0°)$. Results are shown for $L_p/R_p = 0.03$, presenting the distribution of the GND dislocation density ρ_G, the SSD dislocation density ρ_S and the total dislocation density ρ.

The results shown in Fig. 4, where the concentration of hydrogen trapped at dislocation sites $C_T^{(d)}$ is shown for both $L_p = 0.03R_p$ and $L_p = 0$, reveal that the consideration of mechanistic, strain gradient plasticity models can lead to a more significant effect of dislocation trap sites in the vicinity of the crack, relative to conventional plasticity models. For the binding energies and trap densities considered here, the hydrogen trapped at dislocation sites can reach levels of up to 2 wt ppm if the GND contribution to the dislocation trap density is accounted for. In all the coupled deformation-diffusion studies reported so far, the dislocation density is assumed to be that SSDs only, neglecting this important contribution (see, e.g., Sofronis et al., 2001

32

and references therein). The higher C_L levels predicted when $L_p > 0$ are also likely contributing to the higher magnitude of $C_T^{(d)}$, as a higher trap occupancy is attained.
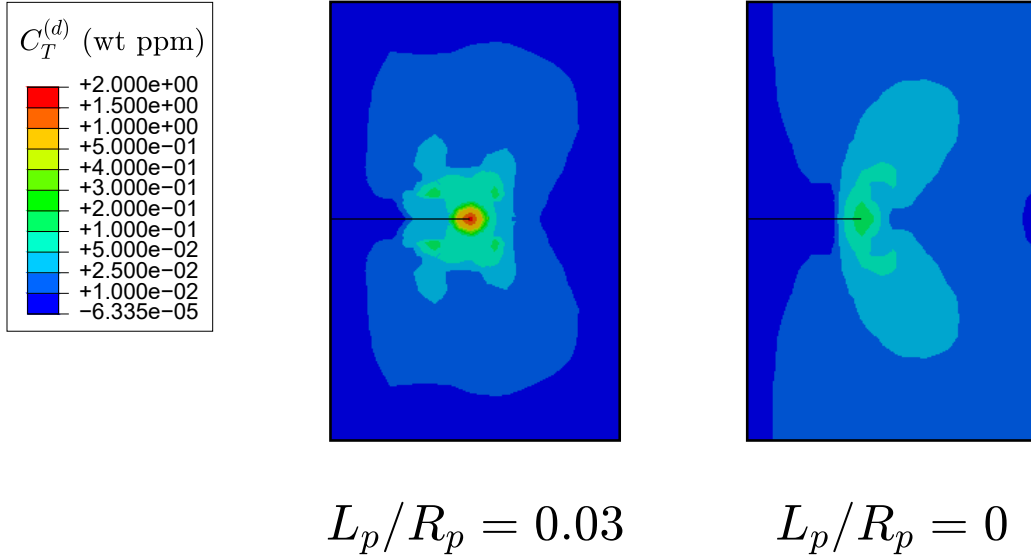

$$L_p/R_p = 0.03 \qquad L_p/R_p = 0$$

Figure 4: Stationary crack tip analysis: Contours of the trapped hydrogen concentration at dislocation sites $C_T^{(d)}$. Results are shown for both mechanism-based strain gradient (MSG) plasticity ($L_p/R_p = 0.03$) and conventional plasticity ($L_p/R_p = 0$).

Now, let us turn attention to crack propagation. The phase field fracture formulation for hydrogen embrittlement described in Section 2.4.2 is taken into consideration. Following (Tvergaard and Hutchinson, 1992; Martínez-Pañeda et al., 2019), for a material with toughness G_c, a reference stress intensity fracture for crack initiation can be defined as,

$$K_0 = \left(\frac{EG_c}{1 - \nu^2} \right)^{1/2}, \tag{69}$$

and a reference size of fracture process zone R_0 reads

$$R_0 = \frac{1}{3\pi (1 - \nu^2)} \frac{EG_c}{\sigma_Y^2}. \tag{70}$$

33

Thus, the relevant non-dimensional group for the phase field fracture process is given by ℓ/R_0. As discussed extensively in Tanné et al. (2018), the choice of a positive $\ell > 0^+$ in the phase field formulation introduces the concept of a material strength $\hat{\sigma}$; e.g., in a one-dimensional setting:

$$\hat{\sigma} = \frac{9}{16}\sqrt{\frac{EG_c}{3\ell}} \tag{71}$$

Accordingly, the phase field length scale ℓ not only acts as a regularising parameter but is attributed a physical meaning. As discussed by Kristensen et al. (2020a), an analogy can then be drawn with cohesive zone analyses based on material cohesive strength $\hat{\sigma}$. Specifically, combining (70) and (71), one reaches,

$$\frac{R_0}{\ell} = \frac{256}{81\pi\left(1 - \nu^2\right)}\left(\frac{\hat{\sigma}}{\sigma_Y}\right)^2. \tag{72}$$

We shall first examine, in the absence of hydrogen, the role of the non-dimensional groups L_p/R_0 and ℓ/R_0 (or $\hat{\sigma}/\sigma_Y$) in the fracture process. The results computed for the case of a varying L_p/R_0 are shown in Fig. 5. Results are presented in terms of a normalised remote load K_I/K_0 versus the normalised crack extension $\Delta a/R_0$. It can be observed that the initiation of crack growth takes place at $K_I = K_0$ (or $G = G_c$) for all cases, in agreement with expectations. However, the degree of dissipation is sensitive to the ratio between the plastic length scale and the fracture process zone. Larger L_p/R_0 values translate into a greater influence of plastic strain gradients and this results in a smaller fracture resistance. Quantitative predictions are thus sensitive to the capacity of the material to strengthen or harden in the presence of plastic strain gradients, characterised *via* L_p, and on the work of fracture, as given by G_c. Also, this necessarily implies that gradient effects

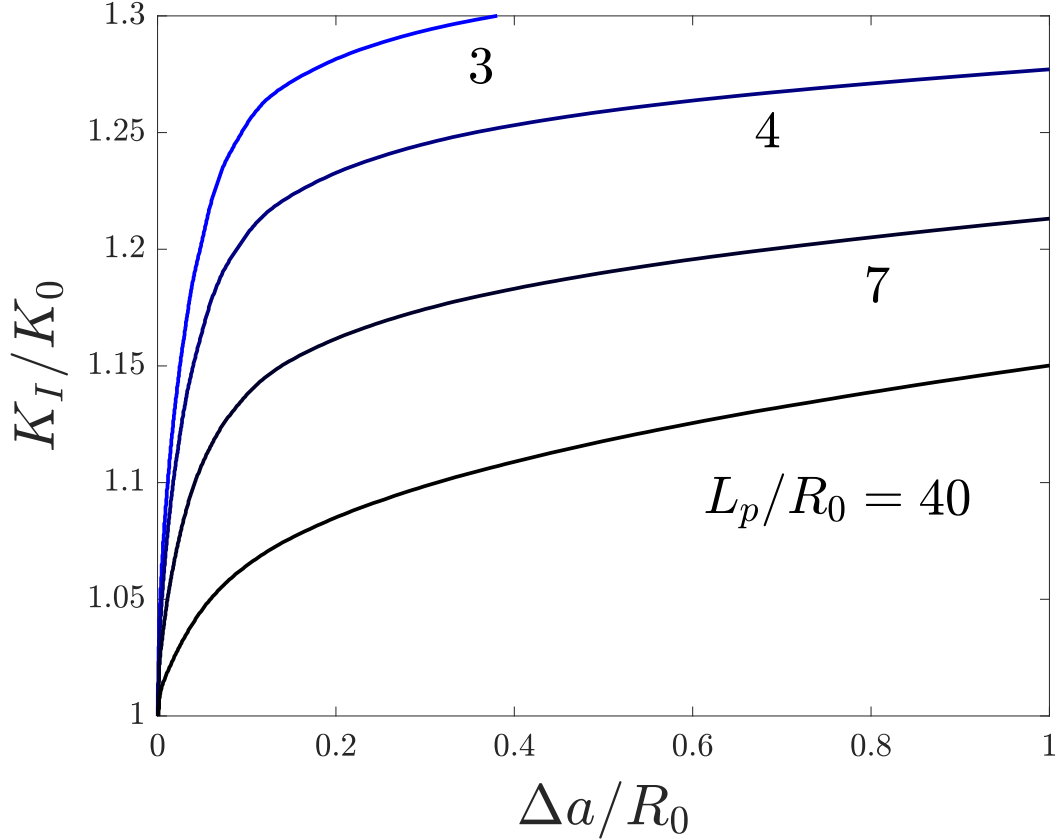have a larger influence in brittle fracture processes, where G_c is small and consequently L_p/R_0 is large.

Figure 5: Influence of the plastic length scale (L_p) on crack growth resistance. Material properties: $\hat{\sigma}/\sigma_y \approx 6\,(\ell/R_0 = 1/40)$, $\sigma_y/E = 0.003$, $\nu = 0.3$, $N = 0.2$.

Consider now a fixed $L_p/R_0 = 40$ and vary the ratio of phase field length scale to fracture process zone size, ℓ/R_0. We emphasise that this is equivalent to varying the material strength $\hat{\sigma}/\sigma_Y$. The results obtained are shown in Fig. 6. Crack growth resistance diminishes with decreasing $\hat{\sigma}/\sigma_Y$ (increasing ℓ/R_0). This agrees with the trends observed in cohesive zone model studies,

where a higher crack growth resistance is observed for larger values of the cohesive strength. The larger the material strength the more plastic dissipation takes place during the crack propagation stage. It is important to note that brittle interfaces, such as grain boundaries, have strength values on the order of $\hat{\sigma}/\sigma_Y \sim 10$ and consequently for brittle fracture to be predicted two conditions must be met: (i) gradient effects must be considered, as otherwise the stress elevation is insufficient, and (ii) the magnitude of G_c has to be small, e.g. through an embrittlement process, so that gradient effects (L_p/R_0) are sufficiently large. In the case of hydrogen embrittlement, there is a dual contribution of the hydrogen in reducing G_c and the interface strength $\hat{\sigma}$, as shown in atomistic simulations (Van der Ven and Ceder, 2003; Jiang and Carter, 2004; Alvaro et al., 2015), which enables predicting decohesion of brittle interfaces if GNDs and dislocation hardening are accounted for. In other words, the combination of strain gradient plasticity, a fracture process zone approach and a degradation of the toughness with hydrogen content provides a modern rationale for hydrogen enhanced decohesion.
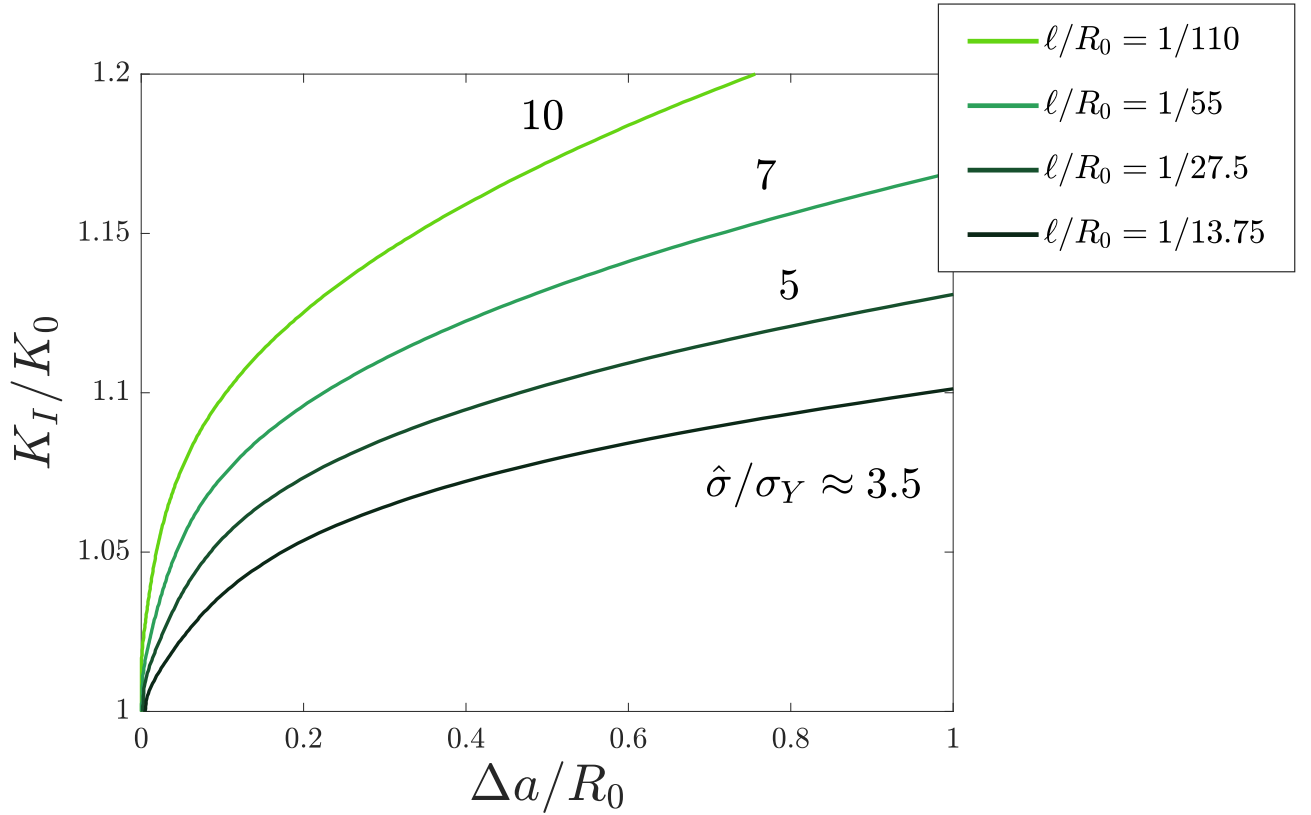
Figure 6: Influence of the material strength $\hat{\sigma}/\sigma_Y$ (ℓ/R_0) on crack growth resistance. Material properties: $\sigma_Y/E = 0.003$, $\nu = 0.3$, $N = 0.2$, and $L_p/R_0 = 40$.

Now, let us explicitly incorporate the influence of hydrogen. For this, a constitutive choice for the hydrogen degradation law remains to be made. A mechanistic, multi-scale approach is adopted for this boundary value problem. The fracture process is assumed to be intergranular, as observed experimentally in many material systems exposed to hydrogen (see, e.g., Banerji et al., 1978; Harris et al., 2018; Pouillier et al., 2012), and thus driven by the hydrogen-assisted decohesion of grain boundaries - the occupancy of grain boundary trap sites $\theta_T^{(gb)}$ is the quantity of interest. A connection with the

atomic scale process of grain boundary decohesion is established defining a degradation law that exhibits the linear decrease in surface energy with increasing hydrogen coverage observed in atomistic calculations (Alvaro et al., 2015; Jiang and Carter, 2004):

$$G_c\left(\theta\right) = \left(1 - \chi\theta_T^{(gb)}\right) G_c\left(0\right) . \tag{73}$$

The parameter χ is a hydrogen damage coefficient, which can be fitted to quantitatively reproduce the atomistic results (Martínez-Pañeda et al., 2018). For example, here we adopt a value of $\chi = 0.89$, which provides a good fit to the Density Functional Theory data for iron (Jiang and Carter, 2004). The hydrogen transport properties are those described for the stationary crack analysis and the loading rate equals $\dot{K}_I/K_0 = 4 \times 10^{-7}$ s^{-1}. Samples are continuously exposed to an environmental hydrogen concentration C_{env} and are exposed to the same environment for a sufficiently long time before mechanical loading is applied, such that $C_L = C_{env} \ \forall \, x$ at $t = 0$. A *moving* chemical boundary condition is applied, as in (Martínez-Pañeda et al., 2020b), to capture how the environment (hydrogen gas or aqueous electrolyte) promptly occupies the space created by crack advance.

The crack growth resistance curves obtained for different hydrogen environments are shown in Fig. 7. The results show a significant decrease in the load for crack initiation with increasing hydrogen content; the initiation of crack growth takes place at K_I values lower than hydrogen-free K_0 (computed from $G_c(0)$). Accordingly, the crack growth resistance also diminishes as the magnitude of C_{env} increases. In addition, it is shown that the fracture of brittle interfaces ($\hat{\sigma}/\sigma_y = 10$) can occur for hydrogen concentrations as

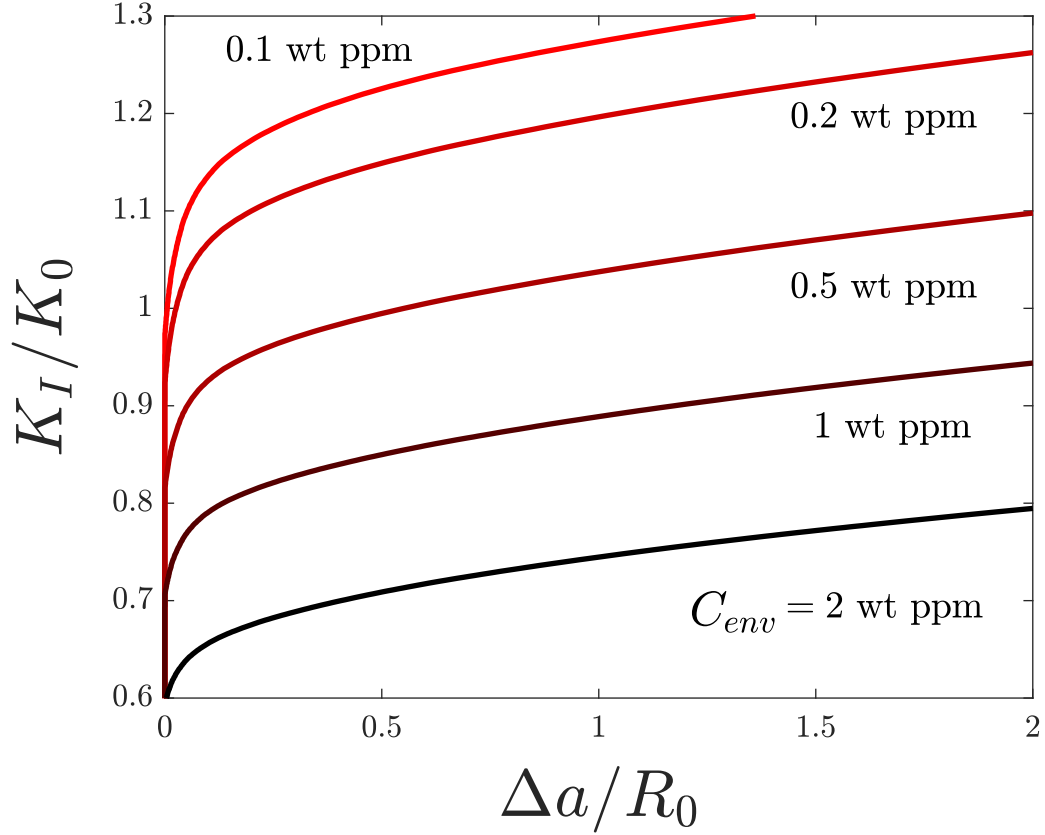low as 0.1 ppm if $L_p/R_0 = 5$.

Figure 7: Effect of the environmental hydrogen concentration on the fracture resistance. Material properties: $\sigma_y/E = 0.003$, $\nu = 0.3$, $N = 0.2$, $\hat{\sigma}/\sigma_y = 10$ ($\ell/R_0 = 1/110$), $L_p/R_0 = 5$, $D = 0.0127$ mm^2/s, and $\chi = 0.89$. Loading rate $\dot{K}_I/K_0 = 4 \times 10^{-7}$ s^{-1}.

Finally, we conclude the crack growth resistance analysis by assessing the influence of the loading rate. In this case, the specimens are pre-charged to a hydrogen content of 0.5 wt ppm but are then subjected to mechanical load in an inert environment, implying the application of a Dirichlet-type boundary condition $C_L = 0$ in the crack surface. As in the hydrogen environmentally assisted cracking example, the $C_L = 0$ condition is enforced at all times at

the crack surfaces by means of a penalty approach. This reflects the fact that the newly created crack surfaces are immediately exposed to an inert environment.
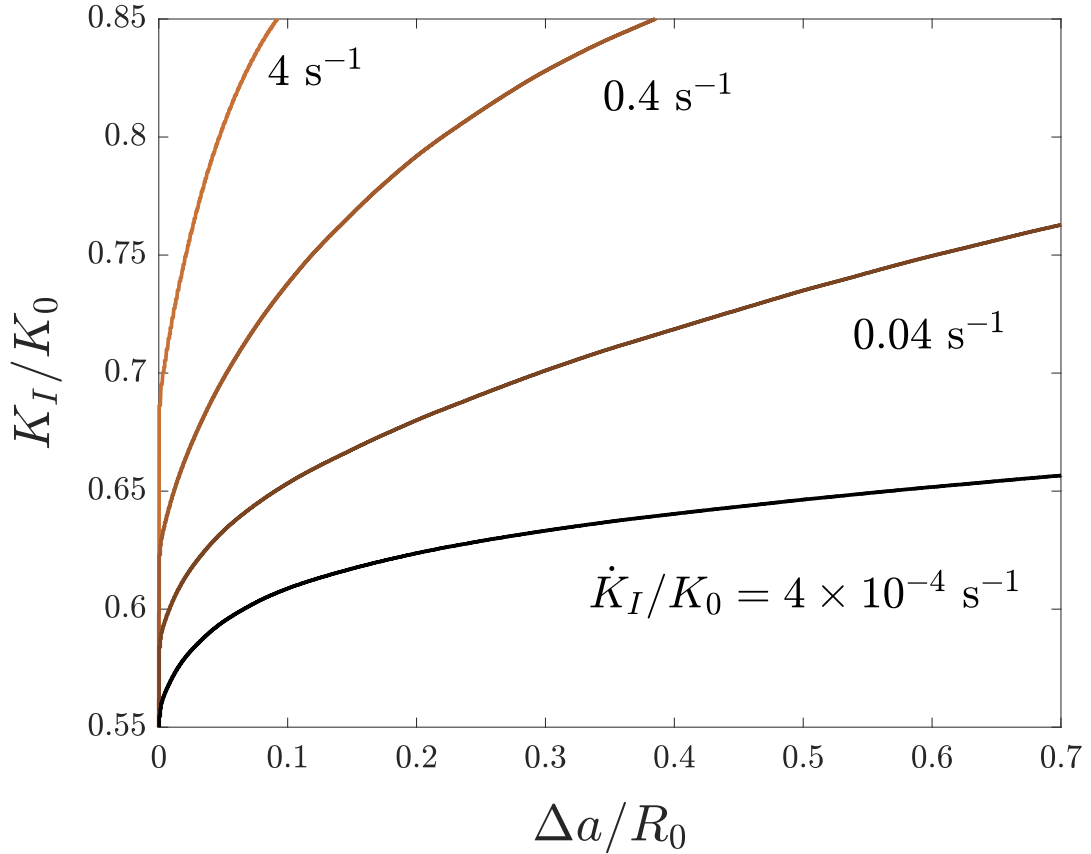

Figure 8: Effect of the loading rate ($\dot{K}_I/K_0$) on the fracture resistance of samples pre-charged with a uniform hydrogen concentration of 0.5 wt ppm. Material properties: $\sigma_y/E = 0.003$, $\nu = 0.3$, $N = 0.2$, $\hat{\sigma}/\sigma_y \approx 6$ ($\ell/R_0 = 0.025$), $L_p/R_0 = 5$, $D = 0.0127$ mm^2/s, and $\chi = 0.89$.

The results obtained varying the loading rate from $\dot{K}_I/K_0 = 4 \times 10^{-7}$ to $\dot{K}_I/K_0 = 4$ s^{-1} are shown in Fig. 8. The results reveal that the model can rigorously capture how hydrogen damage becomes more significant for

smaller loading rates. The smaller the magnitude of $\dot{K}_I/K_0$, the larger the time available for the hydrogen to diffuse to the fracture process zone. The influence is observed over a range of loading rates spanning at least four orders of magnitude, consistent with experimental observations (Momotani et al., 2017).

4.2. Experimental validation: failure of pre-charged AISI 4135 steel bars

We shall now compare model predictions with experimental measurements of failure stress versus hydrogen concentration. The experiments by Wang et al. (2005) on pre-charged notched AISI 4135 steel bars are taken as a benchmark. The geometry and dimensions are given in Fig. 9. The bar is cylindrical and we thus adopt an axisymmetric formulation, modifying the strain-displacement matrix and integrating the discretised equations in polar coordinates. We also take advantage of symmetry and model only half of the plane problem. The model is discretised with a total of 20,373 quadratic quadrilateral axisymmetric elements with reduced integration. The finite element mesh is refined along the crack propagation region, with the characteristic element length being ten times smaller than the phase field length scale, $\ell = 0.029$ mm. The material properties are listed in Table 1. Following Wang et al. (2005), the mechanical properties of the AISI 4135 steel bars are given by a Young's modulus of $E = 210$ GPa, a Poisson's ratio of $\nu = 0.3$, and a yield stress of $\sigma_Y = 1235$ MPa. The work hardening behaviour is captured by reproducing the stress-strain curve reported in (Wang et al., 2005) with the hardening law given in Eq. (26), this fitting exercise renders a strain hardening exponent of $N = 0.05$.
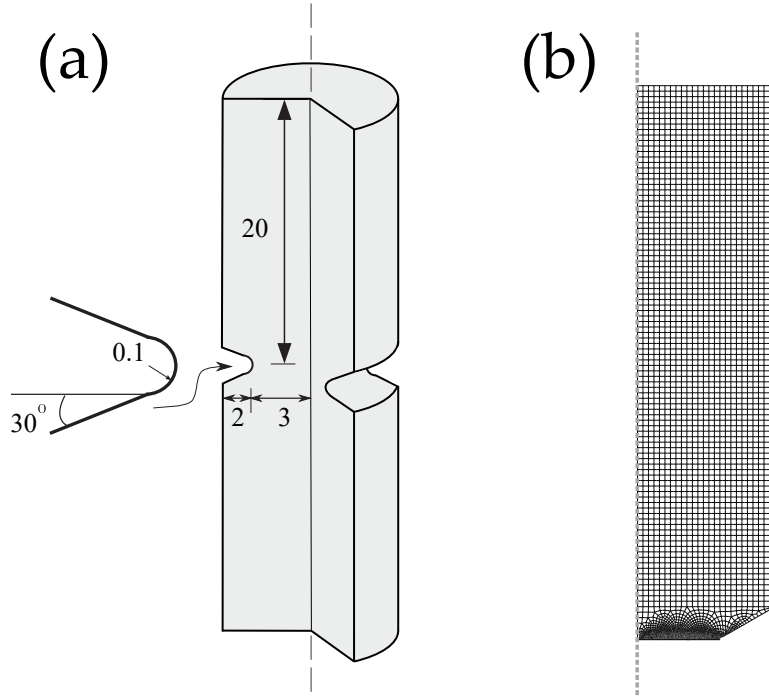
Figure 9: Experimental comparison. Geometry, dimensions (in mm) and finite element mesh for the simulation of notch strength degradation of AISI 4135 steel bars with hydrogen content.

The hydrogen transport properties are also listed in in Table 1. A lattice diffusion coefficient of $D = 3.8 \times 10^{-11}$ m^2/s is considered, as reported in Wang et al. (2005). Also, following their findings, two types of traps are considered: dislocations and grain boundaries. Quantitative values for the density and the binding energy of each trap type are not available. Thus, we take the trapping information from the study by Fernández-Sousa et al. (2020) on AISI 4140 steel. Namely, the grain boundary trap density and binding energy are respectively given by $N_T^{(gb)} = 5.06 \times 10^{25}$ sites/m^3 and $W_B^{(gb)} = -24.7$ kJ/mol. The dislocation trap binding energy is given by

$W_B^{(d)} = -35.2$ kJ/mol, while $N_T^{(d)}$ is estimated from the total dislocation density by using Eq. (48). An initial dislocation density of $\rho_0 = 10^{14}$ m^{-2} is assumed for the unstressed state. Fracture properties are not reported in the benchmark study by Wang et al. (2005). Thus, the material toughness in the absence of hydrogen $G_c(0)$ is estimated by calibrating with the experiment conducted in air: the experimental notch tensile strength is attained with a magnitude of $G_c = 25$ kJ/m^2.

Table 1: Material properties used in the validation with the experiments on pre-charged AISI 4135 steel bars by Wang et al. (2005). The parameters are taken from (Wang et al., 2005) and (Fernández-Sousa et al., 2020).

Parameter	Magnitude
Mechanical properties	
Young's modulus, E	210,000 MPa
Poisson's ratio, ν	0.3
Yield stress, σ_Y	1235 MPa
Strain hardening exponent, N	0.05
Hydrogen transport properties	
Lattice diffusion coefficient, D	3.8×10^{-11} m^2/s
Grain boundary trap density, $N_T^{(gb)}$	5.06×10^{25} sites/m^3
Grain boundary binding energy, $W_B^{(gb)}$	-24.7 kJ/mol
Initial dislocation trap density, $N_T^{(d)}(t=0)$	5.06×10^{25} sites/m^3
Dislocation binding energy, $W_B^{(d)}$	-35.2 kJ/mol

To capture the hydrogen degradation, a phenomenological approach is followed, building upon the experimental data available: sensitivity of the

notch tensile strength σ_f versus pre-charged hydrogen content C_0. First, we conduct a series of virtual experiments in the absence of hydrogen to determine the magnitude of G_c that corresponds to each critical stress value. We then estimate the magnitude of $\theta_T^{(gb)}$ that corresponds to the value of the lattice hydrogen concentration at the beginning of the experiment. Thus, assuming Oriani's equilibrium, the occupancy of grain boundary trapping sites can be determined for a given C_L by considering Eqs. (38) and (39). This allows plotting G_c vs $\theta_T^{(gb)}$, which is accurately fitted with the following law:

$$G_c = G_c(0) \left(3.519 \exp(-103.1\theta_T^{(gb)}) + 0.1567 \exp(-5.572\theta_T^{(gb)}) \right) \tag{74}$$

This two-term exponential relation that provides the best fit to the simulated G_c vs $\theta_T^{(gb)}$ data is introduced into the model, replacing the atomistic law employed in Section 4.1. We proceed then to run a number of deformation-diffusion-fracture computations to determine the notch failure strength as a function of the pre-charged hydrogen content. The strain loading rate equals $\dot{\varepsilon} = 8.3 \times 10^{-7}$ s^{-1}, as in the experiments by Wang et al. (2005). The results obtained are shown in Fig. 10, together with the experimental data.
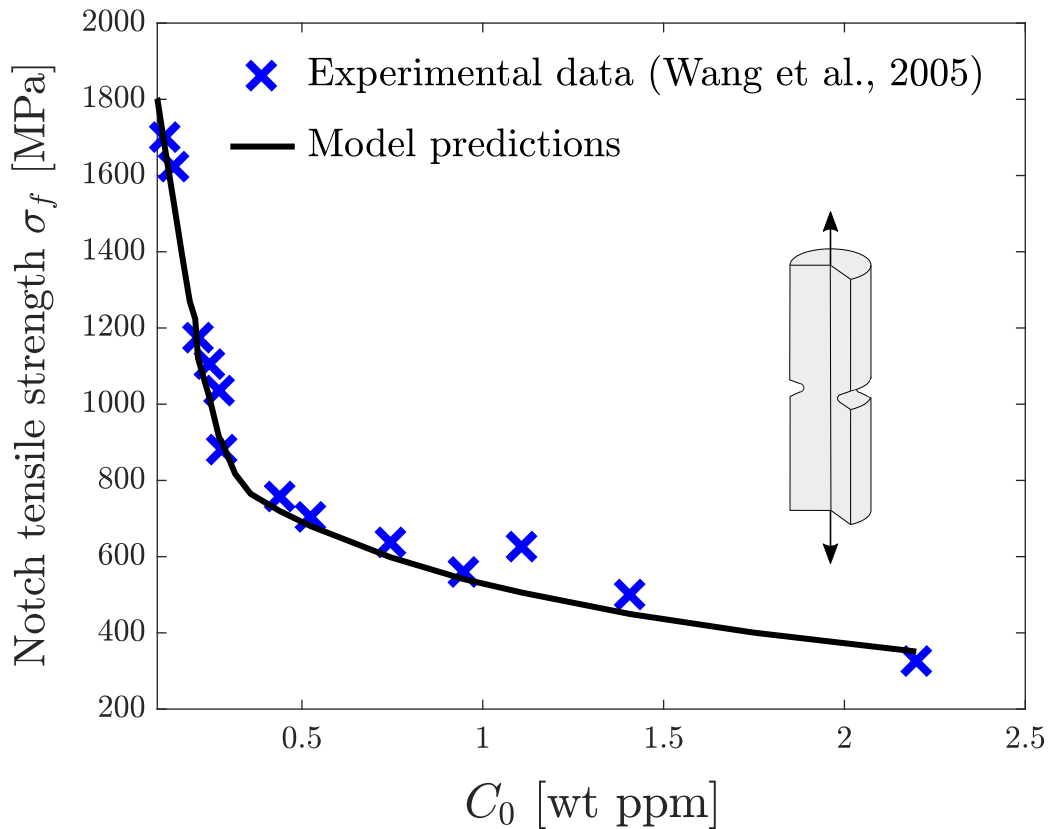
44

Figure 10: Experimental comparison. Predictions of the reduction in tensile strength with pre-charged hydrogen concentration for notched AISI 4135 steel bars. The solid lines denote model predictions (present work) while the symbols correspond to the experimental data reported by Wang et al. (2005).

An excellent agreement with the experimental results by Wang et al. (2005) is obtained. This is not surprising, given the phenomenological approach adopted, where the experimental data is used to construct the degradation law. It is of interest to compare this degradation law with the atomistic one adopted in Section 4.1 - Eq. (73). Values of $\theta_T^{(gb)}$ equal or higher than 0.2 result in a significantly larger degradation for the phenomenological

approach. In fact, Eq. (74) exhibits a sharp drop for small values of $\theta_T^{(gb)}$ (≤ 0.05), followed by a milder slope (relative to the atomistic curve). The phenomenological degradation law is a reflection of the experimental results; as shown (e.g.) in Fig. 1 of (Fernández-Sousa et al., 2020), Oriani's equilibrium dictates that for a trap with binding energy $W_B^{(gb)} = -24.7$ kJ/mol, an occupancy of $\theta_T = 0.05$ is attained for $C_L \approx 0.4$ ppm. Thus, experiments suggest a reduction in notch tensile strength of more than 50% for $\theta_T^{(gb)} = 0.05$. Is such a small occupancy value capable of bringing such a significant reduction in grain boundary strength or are there other mechanisms involved? We note that this analysis is based on the bulk concentration; while this is reasonable for notched samples, the consideration of a small pre-existing crack would lead to much higher local levels of C_L and grain boundary trap occupancy. Also, these estimations are very sensitive to the magnitude of $W_B^{(gb)}$. If the trap binding energy of -35.2 kJ/mol were to be interpreted as that of grain boundaries (as opposed to dislocations), the grain boundary occupancy would be approximately $\theta_T^{(gb)} = 0.7$ for $C_L = 0.4$ ppm, bringing the phenomenological and atomistic laws very close to each other. Undoubtedly, there is a strong need to develop rigorous procedures for quantifying the hydrogen trapping characteristics of metals.

5. Conclusions

We have presented a new mechanistic framework for predicting the embrittlement of metallic components exposed to hydrogen-containing environments. Key features of the model include: (i) a mechanism-based strain gradient constitutive characterisation of crack tip stresses and dislocation den-

46

sities, (ii) a coupled deformation-diffusion transport formulation, accounting for multiple trap types, and (iii) a hydrogen-dependent phase field description of fracture. The model was numerically implemented in the context of the finite element method, with displacements, hydrogen concentration and phase field parameter being the primary kinematic variables. First, stationary cracks were investigated to assess the influence on crack tip mechanics of the Taylor-based constitutive model adopted. Results showed that large plastic strain gradients close to the crack led to crack tip stresses that were notably higher than those predicted using conventional continuum models. We also investigated the interplay between the various length scales involved: the fracture process zone length R_0, the plastic length scale L_p and the phase field length scale ℓ, which governs the material strength. Also, it was shown that the crack growth resistance decreases with increasing strength, as there is a greater degree of plastic dissipation, and with L_p/R_0, as gradient effects become more significant. Thirdly, model predictions were benchmarked against experiments on cylindrical notched bars made of AISI 4135 steel, which were pre-charged with different levels of hydrogen content. The results showed that the model can quantitatively capture how the notch tensile strength drops with increasing hydrogen concentration. During the analyses, two options were considered to define the degradation of the material toughness with hydrogen: (i) a *first principles* approach, in which atomistic calculations are used to establish the relation between fracture energy and hydrogen coverage, and (ii) a new phenomenological procedure, which is based on experimental data but does not require conducting coupled simulations. It was shown that both approaches led to a similar sensitivity of

the fracture energy to hydrogen coverage if grain boundary cracking drives embrittlement and if the grain boundary trap binding energy lies within the range of -35 to -40 kJ/mol. These results highlight the need for an accurate characterisation of the hydrogen diffusion energy landscape.

6. Acknowledgements

References

Alvaro, A., Thue Jensen, I., Kheradmand, N., Løvvik, O.M., Olden, V., 2015. Hydrogen embrittlement in nickel, visited by first principles modeling, cohesive zone simulation and nanomechanical testing. International Journal of Hydrogen Energy 40, 16892–16900.

Ambati, M., Gerasimov, T., De Lorenzis, L., 2015. A review on phase-field models of brittle fracture and a new fast hybrid formulation. Computational Mechanics 55, 383–405.

Amor, H., Marigo, J.J., Maurini, C., 2009. Regularized formulation of the variational brittle fracture with unilateral contact: Numerical experiments. Journal of the Mechanics and Physics of Solids 57, 1209–1229.

Anand, L., Mao, Y., Talamini, B., 2019. On modeling fracture of ferritic steels due to hydrogen embrittlement. Journal of the Mechanics and Physics of Solids 122, 280–314.

Arsenlis, A., Parks, D.M., 1999. Crystallographic aspects of geometrically-necessary and statistically-stored dislocation density. Acta Materialia 47, 1597–1611.

Banerji, S.K., McMahon, C.J., Feng, H.C., 1978. Intergranular fracture in 4340-type steels: Effects of impurities and hydrogen. Metallurgical Transactions A 9, 237–247.

Barrera, O., Tarleton, E., Tang, H.W., Cocks, A.C.F., 2016. Modelling the coupling between hydrogen diffusion and the mechanical behaviour of metals. Computational Materials Science 122, 219–228.

Bellettini, G., Coscia, A., 1994. Discrete approximation of a free discontinuity problem. Numerical Functional Analysis and Optimization 15, 201–224.

Borden, M.J., Hughes, T.J.R., Landis, C.M., Anvari, A., Lee, I.J., 2016. A phase-field formulation for fracture in ductile materials: Finite deformation balance law derivation, plastic degradation, and stress triaxiality effects. Computer Methods in Applied Mechanics and Engineering 312, 130–166.

Bourdin, B., Francfort, G.A., Marigo, J.J., 2000. Numerical experiments in revisited brittle fracture. Journal of the Mechanics and Physics of Solids 48, 797–826.

del Busto, S., Betegón, C., Martínez-Pañeda, E., 2017. A cohesive zone framework for environmentally assisted fatigue. Engineering Fracture Mechanics 185, 210–226.

Chambolle, A., 2004. An approximation result for special functions with

bounded deformation. Journal des Mathematiques Pures et Appliquees 83, 929–954.

Cui, C., Ma, R., Martínez-Pañeda, E., 2021. A phase field formulation for dissolution-driven stress corrosion cracking. Journal of the Mechanics and Physics of Solids 147, 104254.

Dadfarnia, M., Novak, P., Ahn, D.C., Liu, J.B., Sofronis, P., Johnson, D.D., Robertson, I.M., 2010. Recent advances in the study of structural materials compatibility with hydrogen. Advanced Materials 22, 1128–1135.

Dadfarnia, M., Sofronis, P., Neeraj, T., 2011. Hydrogen interaction with multiple traps: Can it be used to mitigate embrittlement? International Journal of Hydrogen Energy 36, 10141–10148.

Davey, W.P., 1925. Precision measurements of the lattice constants of twelve common metals. Physical Review 25, 753–761.

Di Leo, C.V., Anand, L., 2013. Hydrogen in metals: A coupled theory for species diffusion and large elastic-plastic deformations. International Journal of Plasticity 43, 42–69.

Díaz, A., Alegre, J.M., Cuesta, I.I., 2016. Coupled hydrogen diffusion simulation using a heat transfer analogy. International Journal of Mechanical Sciences 115-116, 360–369.

Djukic, M.B., Bakic, G.M., Sijacki Zeravcic, V., Sedmak, A., Rajicic, B., 2019. The synergistic action and interplay of hydrogen embrittlement mechanisms in steels and iron: Localized plasticity and decohesion. Engineering Fracture Mechanics 216, 106528.

Duda, F.P., Ciarbonetti, A., Sánchez, P.J., Huespe, A.E., 2015. A phase-field/gradient damage model for brittle fracture in elastic-plastic solids. International Journal of Plasticity 65, 269–296.

Duda, F.P., Ciarbonetti, A., Toro, S., Huespe, A.E., 2018. A phase-field model for solute-assisted brittle fracture in elastic-plastic solids. International Journal of Plasticity 102, 16–40.

Elmukashfi, E., Tarleton, E., Cocks, A.C.F., 2020. A modelling framework for coupled hydrogen diffusion and mechanical behaviour of engineering components. Computational Mechanics 66, 189–220.

Fernández-Sousa, R., Betegón, C., Martínez-Pañeda, E., 2020. Analysis of the influence of microstructural traps on hydrogen assisted fatigue. Acta Materialia 199, 253–263.

Fleck, N.A., Hutchinson, J.W., 1997. Strain gradient plasticity. Advances in Applied Mechanics 33, 295–361.

Fleck, N.A., Muller, G.M., Ashby, M.F., Hutchinson, J.W., 1994. Strain gradient plasticity: Theory and Experiment. Acta Metallurgica et Materialia 42, 475–487.

Gangloff, R.P., 2003. Hydrogen-assisted Cracking, in: Milne, I., Ritchie, R., Karihaloo, B. (Eds.), Comprehensive Structural Integrity Vol. 6. Elsevier Science, New York, NY, pp. 31–101.

Gangloff, R.P., Somerday, B.P., 2012. Gaseous Hydrogen Embrittlement of Materials in Energy Technologies. Woodhead Publishing Limited, Cambridge.

Gao, H., Hang, Y., Nix, W.D., Hutchinson, J.W., 1999. Mechanism-based strain gradient plasticity - I. Theory. Journal of the Mechanics and Physics of Solids 47, 1239–1263.

Gurtin, M.E., Anand, L., 2005. A theory of strain-gradient plasticity for isotropic, plastically irrotational materials. Part II: Finite deformations. International Journal of Plasticity 21, 2297–2318.

Gurtin, M.E., Fried, E., Anand, L., 2010. The Mechanics and Thermodynamics of continua. Cambridge University Press, Cambridge, UK.

Harris, Z.D., Lawrence, S.K., Medlin, D.L., Guetard, G., Burns, J.T., Somerday, B.P., 2018. Elucidating the contribution of mobile hydrogen-deformation interactions to hydrogen-induced intergranular cracking in polycrystalline nickel. Acta Materialia 158, 180–192.

Hirshikesh, Natarajan, S., Annabattula, R.K., Martínez-Pañeda, E., 2019. Phase field modelling of crack propagation in functionally graded materials. Composites Part B: Engineering 169, 239–248.

Hirth, J.P., 1980. Effects of hydrogen on the properties of iron and steel. Metallurgical Transactions A 11, 861–890.

Huang, Y., Qu, S., Hwang, K.C., Li, M., Gao, H., Huang, Y., Qu, S., Hwang, K.C., Li, M., Gao, H., 2004. A conventional theory of mechanism-based strain gradient plasticity. International Journal of Plasticity 20, 753–782.

Hutchinson, J.W., 1983. Fundamentals of the phenomenological theory of nonlinear fracture mechanics. Journal of Applied Mechanics, Transactions ASME 50, 1042–1051.

Jiang, D.E., Carter, E.A., 2004. First principles assessment of ideal fracture energies of materials with mobile impurities: Implications for hydrogen embrittlement of metals. Acta Materialia 52, 4801–4807.

Kehler, B.A., Scully, J.R., 2008. Predicting the effect of applied potential on crack tip hydrogen concentration in low-alloy martensitic steels. Corrosion 64, 465–477.

Kiuchi, K., McLellan, R.B., 1983. The solubility and diffusivity of hydrogen in well-annealed and deformed iron. Acta Metallurgica 31, 961–984.

Kok, S., Beaudoin, A.J., Tortorelli, D.A., 2002. A polycrystal plasticity model based on the mechanical threshold. International Journal of Plasticity 18, 715–741.

Komaragiri, U., Agnew, S.R., Gangloff, R.P., Begley, M.R., 2008. The role of macroscopic hardening and individual length-scales on crack tip stress elevation from phenomenological strain gradient plasticity. Journal of the Mechanics and Physics of Solids 56, 3527–3540.

Kristensen, P.K., Martínez-Pañeda, E., 2020. Phase field fracture modelling using quasi-Newton methods and a new adaptive step scheme. Theoretical and Applied Fracture Mechanics 107, 102446.

Kristensen, P.K., Niordson, C.F., Martínez-Pañeda, E., 2020a. A phase field model for elastic-gradient-plastic solids undergoing hydrogen embrittlement. Journal of the Mechanics and Physics of Solids 143, 104093.

Kristensen, P.K., Niordson, C.F., Martínez-Pañeda, E., 2020b. Applications

of phase field fracture in modelling hydrogen assisted failures. Theoretical and Applied Fracture Mechanics 110, 102837.

Kumar, R., Mahajan, D.K., 2020. Hydrogen distribution in metallic polycrystals with deformation. Journal of the Mechanics and Physics of Solids 135, 103776.

Li, D., Gangloff, R.P., Scully, J.R., 2004. Hydrogen Trap States in Ultrahigh-Strength AERMET 100 Steel. Metallurgical and Materials Transactions A: Physical Metallurgy and Materials Science 35 A, 849–864.

Liu, B., Huang, Y., Li, M., Hwang, K.C., Liu, C., 2005. A study of the void size effect based on the Taylor dislocation model. International Journal of Plasticity 21, 2107–2122.

Lufrano, J., Sofronis, P., Birnbaum, H.K., 1998. Elastoplastically accommodated hydride formation and embrittlement. Journal of the Mechanics and Physics of Solids 46, 1497–1520.

Lynch, S., 2019. Discussion of some recent literature on hydrogen-embrittlement mechanisms: Addressing common misunderstandings. Corrosion Reviews 37, 377–395.

Martínez-Pañeda, E., Betegón, C., 2015. Modeling damage and fracture within strain-gradient plasticity. International Journal of Solids and Structures 59, 208–215.

Martínez-Pañeda, E., del Busto, S., Betegón, C., 2017. Non-local plasticity effects on notch fracture mechanics. Theoretical and Applied Fracture Mechanics 92, 276–287.

Martínez-Pañeda, E., Deshpande, V.S., Niordson, C.F., Fleck, N.A., 2019. The role of plastic strain gradients in the crack growth resistance of metals. Journal of the Mechanics and Physics of Solids 126, 136–150.

Martínez-Pañeda, E., Díaz, A., Wright, L., Turnbull, A., 2020a. Generalised boundary conditions for hydrogen transport at crack tips. Corrosion Science 173, 108698.

Martínez-Pañeda, E., Fleck, N.A., 2019. Mode I crack tip fields: Strain gradient plasticity theory versus J2 flow theory. European Journal of Mechanics - A/Solids 75, 381–388.

Martínez-Pañeda, E., Golahmar, A., Niordson, C.F., 2018. A phase field formulation for hydrogen assisted cracking. Computer Methods in Applied Mechanics and Engineering 342, 742–761.

Martínez-Pañeda, E., Harris, Z.D., Fuentes-Alonso, S., Scully, J.R., Burns, J.T., 2020b. On the suitability of slow strain rate tensile testing for assessing hydrogen embrittlement susceptibility. Corrosion Science 163, 108291.

Martínez-Pañeda, E., Niordson, C.F., 2016. On fracture in finite strain gradient plasticity. International Journal of Plasticity 80, 154–167.

Martínez-Pañeda, E., Niordson, C.F., Gangloff, R.P., 2016. Strain gradient plasticity-based modeling of hydrogen environment assisted cracking. Acta Materialia 117, 321–332.

McAuliffe, C., Waisman, H., 2015. A unified model for metal failure capturing shear banding and fracture. International Journal of Plasticity 65, 131–151.

Miehe, C., Aldakheel, F., Raina, A., 2016. Phase field modeling of ductile fracture at finite strains: A variational gradient-extended plasticity-damage theory. International Journal of Plasticity 84, 1–32.

Miehe, C., Hofacker, M., Welschinger, F., 2010. A phase field model for rate-independent crack propagation: Robust algorithmic implementation based on operator splits. Computer Methods in Applied Mechanics and Engineering 199, 2765–2778.

Momotani, Y., Shibata, A., Terada, D., Tsuji, N., 2017. Effect of strain rate on hydrogen embrittlement in low-carbon martensitic steel. International Journal of Hydrogen Energy 42, 3371–3379.

Mu, Y., Hutchinson, J.W., Meng, W.J., 2014. Micro-pillar measurements of plasticity in confined Cu thin films. Extreme Mechanics Letters 1, 62–69.

Nix, W.D., Gao, H.J., 1998. Indentation size effects in crystalline materials: A law for strain gradient plasticity. Journal of the Mechanics and Physics of Solids 46, 411–425.

Oriani, R.A., Josephic, P.H., 1974. Equilibrium Aspects of Hydrogen Induced Cracking of Steels. Acta Metallurgica 22, 1065–1074.

Orowan, E., 1948. Fracture and Strength of Solids. Reports on Progress in Physics XII, 185.

Papazafeiropoulos, G., Muñiz-Calvente, M., Martínez-Pañeda, E., 2017. Abaqus2Matlab: A suitable tool for finite element post-processing. Advances in Engineering Software 105, 9–16.

Paxton, T., Sutton, A.P., Finnis, M.W., 2017. The challenges of hydrogen and metals. Philosophical Transactions of the Royal Society A: Mathematical, Physical and Engineering Sciences 375.

Pouillier, E., Gourgues, A.F., Tanguy, D., Busso, E.P., 2012. A study of intergranular fracture in an aluminium alloy due to hydrogen embrittlement. International Journal of Plasticity 34, 139–153.

Provatas, N., Elder, K., 2011. Phase-Field Methods in Materials Science and Engineering. John Wiley & Sons, Weinheim, Germany.

Qu, S., Huang, Y., Jiang, H., Liu, C., Wu, P.D., Hwang, K.C., 2004. Fracture analysis in the conventional theory of mechanism-based strain gradient (CMSG) plasticity. International Journal of Fracture 129, 199–220.

Quintanas-Corominas, A., Turon, A., Reinoso, J., Casoni, E., Paggi, M., Mayugo, J.A., 2020. A phase field approach enhanced with a cohesive zone model for modeling delamination induced by matrix cracking. Computer Methods in Applied Mechanics and Engineering 358, 112618.

Serebrinsky, S., Carter, E.A., Ortiz, M., 2004. A quantum-mechanically informed continuum model of hydrogen embrittlement. Journal of the Mechanics and Physics of Solids 52, 2403–2430.

Shi, M., Huang, Y., Jiang, H., Hwang, K.C., Li, M., 2001. The boundary-layer effect on the crack tip field in mechanism-based strain gradient plasticity. International Journal of Fracture 112, 23–41.

Shi, M.X., Huang, Y., Gao, H., 2004. The J-integral and geometrically

necessary dislocations in nonuniform plastic deformation. International Journal of Plasticity 20, 1739–1762.

Shishvan, S.S., Csányi, G., Deshpande, V.S., 2020. Hydrogen induced fast-fracture. Journal of the Mechanics and Physics of Solids 134, 103740.

Simoes, M., Martínez-Pañeda, E., 2021. Phase field modelling of fracture and fatigue in Shape Memory Alloys. Computer Methods in Applied Mechanics and Engineering 373, 113504.

Sofronis, P., Liang, Y., Aravas, N., 2001. Hydrogen induced shear localization of the plastic flow in metals and alloys. Eur. J. Mech. A/Solids 20, 857–872.

Sofronis, P., McMeeking, R.M., 1989. Numerical analysis of hydrogen transport near a blunting crack tip. Journal of the Mechanics and Physics of Solids 37, 317–350.

Tanné, E., Li, T., Bourdin, B., Marigo, J.J., Maurini, C., 2018. Crack nucleation in variational phase-field models of brittle fracture. Journal of the Mechanics and Physics of Solids 110, 80–99.

Taylor, G.I., 1938. Plastic strain in metals. Journal of the Institute of Metals 62, 307–324.

Turnbull, A., 2015. Perspectives on hydrogen uptake, diffusion and trapping. International Journal of Hydrogen Energy 40, 16961–16970.

Tvergaard, V., Hutchinson, J.W., 1992. The relation between crack growth resistance and fracture process parameters in elastic-plastic solids. Journal of the Mechanics and Physics of Solids 40, 1377–1397.

Tvergaard, V., Niordson, C.F., 2004. Nonlocal plasticity effects on interaction of different size voids. International Journal of Plasticity 20, 107–120.

Van der Ven, A., Ceder, G., 2003. Impurity-induced van der Waals transition during decohesion. Physical Review B - Condensed Matter and Materials Physics 67, 1–4.

Van Leeuwen, H.P., 1974. The kinetics of hydrogen embrittlement: A quantitative diffusion model. Engineering Fracture Mechanics 6, 141–161.

Voyiadjis, G.Z., Song, Y., 2019. Strain gradient continuum plasticity theories: Theoretical, numerical and experimental investigations. International Journal of Plasticity 121, 21–75.

Wang, M., Akiyama, E., Tsuzaki, K., 2005. Effect of hydrogen and stress concentration on the notch tensile strength of AISI 4135 steel. Materials Science and Engineering A 398, 37–46.

Wei, Y., Hutchinson, J.W., 1997. Steady-state crack growth and work of fracture for solids characterized by strain gradient plasticity. Journal of the Mechanics and Physics of Solids 45, 1253–1273.

Wei, Y., Xu, G., 2005. A multiscale model for the ductile fracture of crystalline materials. International Journal of Plasticity 21, 2123–2149.

Williams, M.L., 1957. On the stress distribution at the base of a stationary crack. Journal of Applied Mechanics 24, 109–114.

Wu, J.Y., Mandal, T.K., Nguyen, V.P., 2020a. A phase-field regularized

cohesive zone model for hydrogen assisted cracking. Computer Methods in Applied Mechanics and Engineering 358, 112614.

Wu, J.Y., Nguyen, V.P., Nguyen, C.T., Sutula, D., Sinaie, S., Bordas, S., 2020b. Phase-field modelling of fracture. Advances in Applied Mechanics 53, 1–183.

You, T., Waisman, H., Zhu, Q.Z., 2021. Brittle-ductile failure transition in geomaterials modeled by a modified phase-field method with a varying damage-driving energy coefficient. International Journal of Plasticity 136, 102836.

Yu, H., Olsen, J.S., Alvaro, A., Olden, V., He, J., Zhang, Z., 2016. A uniform hydrogen degradation law for high strength steels. Engineering Fracture Mechanics 157, 56–71.